NEW TECHNIQUES FOR IMAGING, DIGITIZATION AND ANALYSIS OF THREE-DIMENSIONAL NEURAL MORPHOLOGY ON MULTIPLE SCALES

S. L. WEARNE,[a,b,c*] A. RODRIGUEZ,[a,d]
D. B. EHLENBERGER,[a,b,c] A. B. ROCHER[a,c]
S. C. HENDERSON[a,e] AND P. R. HOF[a,c*]

[a]*Computational Neurobiology and Imaging Center, Mount Sinai School of Medicine, New York, NY 10029, USA*

[b]*Department of Biomathematical Sciences, Mount Sinai School of Medicine, New York, NY 10029, USA*

[c]*Department of Neuroscience, Mount Sinai School of Medicine, New York, NY 10029, USA*

[d]*Program in Bioinformatics, Boston University, Boston, MA 02215, USA*

[e]*Department of Anatomy and Neurobiology, Virginia Commonwealth University, School of Medicine, Richmond, VA 23298, USA*

Abstract—Cognitive impairment in normal aging and neurodegenerative diseases is accompanied by altered morphologies on multiple scales. Understanding of the role of these structural changes in producing functional deficits in brain aging and neuropsychiatric disorders requires accurate three-dimensional representations of neuronal morphology, and realistic biophysical modeling that can directly relate structural changes to altered neuronal firing patterns. To date however, tools capable of resolving, digitizing and analyzing neuronal morphology on both local and global scales, and with sufficient throughput and automation, have been lacking. The precision of existing image analysis-based morphometric tools is restricted at the finest scales, where resolution of fine dendritic features and spine geometry is limited by the skeletonization methods used, and by quantization errors arising from insufficient imaging resolution. We are developing techniques for imaging, reconstruction and analysis of neuronal morphology that capture both local and global structural variation. To minimize quantization error and evaluate more precisely the fine geometry of dendrites and spines, we introduce a new shape analysis technique, the Rayburst sampling algorithm that uses the original grayscale data rather than the segmented images for precise, continuous radius estimation, and multidirectional radius sampling to represent non-circular branch cross-sections and anisotropic structures such as dendritic spine heads, with greater accuracy. We apply the Rayburst technique to 3D neuronal shape analysis at different scales. We reconstruct and digitize entire neurons from stacks of laser-scanning microscopy images, as well as globally complex structures such as multineuron networks and microvascular networks. We also introduce imaging techniques necessary to recover detailed information on three-dimensional mass distribution and surface roughness of amyloid beta plaques from human Alzheimer's disease patients and from the Tg2576 mouse that expresses the "Swedish" mutation of the amyloid precursor protein.

By providing true three-dimensional morphometry of complex histologic structures on multiple scales, the tools described in this report will enable multiscale biophysical modeling studies capable of testing potential mechanisms by which altered dendritic structure, spine geometry and network branching patterns that occur in normal aging and in many brain disorders, determine deficits of functions such as working memory and cognition. © 2005 IBRO. Published by Elsevier Ltd. All rights reserved.

Key words: confocal laser scanning microscopy, computational neurobiology, image analysis, dendritic spines, neurodegenerative disorders, microvasculature.

*Correspondence to: S. L. Wearne, Department of Neuroscience, Mount Sinai School of Medicine, Box 1065, One Gustave L. Levy Place, New York, NY 10029–6574, USA. Tel: +1-212-659-5572; fax: +1-212-996-9785.
*Correspondence to: P. R. Hof, Department of Neuroscience, Mount Sinai School of Medicine, Box 1065, One Gustave L. Levy Place, New York, NY 10029–6574, USA. Tel: +1-212-659-5904; fax: +1-212-849-2510.
E-mail addresses: susan@camelot.mssm.edu (S. L. Wearne), patrick.hof@mssm.edu (P. R. Hof).
Abbreviations: AD, Alzheimer's disease; CLSM, confocal laser-scanning microscopy/microscope; DAPI, 4,6-diamidino-2-phenylindole; DLA, diffusion-limited aggregation; eGFP, enhanced green fluorescent protein; MLBD, median lower band diameter; MPLSM, multiphoton laser-scanning microscopy; n.a., numerical aperture; VIAS, Volume Integration and Alignment System; WD, working distance; 2D, two-dimensional; 3D, three-dimensional.

We are developing high-resolution three-dimensional (3D) techniques for analyzing the structural basis of impaired neural transmission and plasticity that underlies cognitive decline in normal aging and neurodegenerative disease. Such pathologic states are characterized by a progressive decline in memory-related cognitive abilities (Albert, 1996; Du et al., 2001; Chetelat et al., 2002; Small et al., 2002) and are accompanied by morphologic changes on multiple scales, from the fine-grained geometry of individual neurons, dendrites and spines (Anderson and Rutledge, 1996; de Brabander et al., 1998; Duan et al., 2000, 2003; Page et al., 2002; Jacobs et al., 2001; Hao et al., 2004; Hof and Morrison, 2004; Radley et al., 2005) to the spatial complexity of multineuron and vascular networks in the presence of space-occupying histopathologic lesions (Le et al., 2001; Stern et al., 2004). Inferring mechanisms by which these structural changes bring about the observed cognitive deficits requires a combination of precise 3D morphometry and biophysical modeling that can reliably represent both global dendritic structure and detailed spine geometry. Theoretical and technological developments over the past decades now allow for realistic modeling of structure–function relationships on multiple scales. The application of cable theory (Rall, 1962, 1964) to multi-compartment modeling (Holmes and Rall, 1992; Hines,

1994; Bower and Beeman, 1998; Koch, 1999) for example, permits simulation of voltage spread throughout a branching dendritic tree of arbitrary complexity. High-resolution laser-scanning microscopy can resolve structures on scales ranging from entire neurons to dendritic spines spanning less than a micrometer. With the increasing speed of standard laboratory computers, digitizing, reconstructing and simulating these structures no longer requires supercomputing resources, and will become an increasingly important tool in understanding the structural determinants of normal and pathologic neuronal function.

At the single cell level, dendritic morphology is a fundamental determinant of synaptic integration and neural firing patterns (Mainen and Sejnowski, 1996; Stuart et al., 1999; Koch and Segev, 2000; Euler and Denk, 2001; Vetter et al., 2001; Henry et al., 2002; Krichmar et al., 2002; Ascoli, 2003; Häusser and Mel, 2003). Dendritic arborization patterns provide a substrate both for spatiotemporal integration of multiple inputs and the connectivity patterns that shape network dynamics. Compartmental modeling studies have demonstrated that model neurons with common ion distributions, differing only in the extent of arborization of their dendritic geometries, can reproduce the full range of firing patterns observed experimentally (Mainen and Sejnowski, 1996). Importantly, since both macroscopic branching topology and microscopic surface irregularities including dendritic varicosities (Surkis et al., 1998) and spine density, shape and distribution (Wilson, 1988; Holmes, 1989; Stratford et al., 1989; Baer and Rinzel, 1991; Tsay and Yuste, 2001; Yuste and Bonhoeffer, 2001; Nimchinsky et al., 2002) contribute to the normal case, accurate reconstruction and analysis of 3D structural alterations in neurodegenerative disease are essential to understanding the etiology of impaired cognitive function that accompanies such pathology.

While the gross morphologic effects of neurodegenerative disease have been well documented by stereologic approaches, alterations in fine-grained single neuron morphology and the global topology of multineuron and vascular networks remain poorly characterized. Accumulating data indicate that these more complex morphologic changes, and their interactions, are essential to understanding the spatiotemporal progress of neurodegenerative diseases (Le et al., 2001; Urbanc et al., 2002; D'Amore et al., 2003; Tsai et al., 2004). In Alzheimer's disease (AD) for example, amyloid beta protein exists in many molecular forms, and eventually aggregates into the insoluble plaques that are one of the neuropathological hallmarks of AD. Insoluble amyloid deposits comprising extracellular accumulations of amyloid beta peptide and other proteins surrounded by degenerating axons and dystrophic dendrites are an example of general histopathologic lesions that can physically distort neuronal processes in their vicinity, which must take tortuous routes around the lesions, resulting in characteristic distortions of local and global dendritic geometry (Knowles et al., 1999; Le et al., 2001; Urbanc et al., 2002). In addition, spines are often lost as spiny dendrites traverse a plaque, dendritic shafts undergo atrophy and axons in the vicinity of plaques develop vari-

cosities (Tsai et al., 2004). These distortions and nonhomogeneous degenerative processes have not been quantified in 3D, and their effects on neuronal function are not known.

Severe vascular modifications are also detected in several neurodegenerative disorders (Buée et al., 1994; Bailey et al., 2004). Electron microscopy studies have revealed thickening and vacuolization of the vascular basement membrane, thinning of microvessels referred to as atrophic or string vessels (Bell and Ball, 1981), increased tortuosity (Fischer et al., 1990), and fragmentation of the microvasculature related to a decrease in the number of long microvessels and their branches (Buée et al., 1994). Many microvascular abnormalities occur prior to the development of clinical dementia and to the formation of the characteristic neuronal AD-type lesions (Buée et al., 1994; Keuker et al., 2000), emphasizing the importance of characterizing the spatiotemporal interactions of these alterations.

Current techniques for digitizing neuronal morphology in 3D entail manual tracing using custom packages such as NeuroZoom (Bloom et al., 1997) or Neurolucida (MicroBrightField, Williston, VT, USA). Such methods introduce systematic inaccuracies depending upon the individual performing the tracing, and fail to capture fine dendritic structure including varicosities, continuous taper and spine morphology. In particular, spines are represented as points, labeled independently of the dendritic tracing with a marker of uniform size. Relative diameters of spine heads and necks cannot currently be resolved with these software applications. While a few techniques of varying degrees of automation have been suggested for digitizing neuronal morphology from laser-scanning microscopy images (Streekstra et al., 1999, 2000; Messerli, 2000; He et al., 2003; Schmitt et al., 2004; and see van Pelt et al., 2001 for review), the limited size of the data sets that can be handled, and the general requirement for extensive manual editing renders these impractical in most cases for reconstructing entire neurons or multicellular structures at high resolution. New developments in image analysis and visualization are needed to provide faster, more accurate adaptive segmentation and automatic reconstruction with minimal user interaction, for use with large data sets. A particular problem with existing image analysis-based morphometric tools is their restricted precision at the finest scales, where resolution of fine dendritic features and spine geometry is limited by the skeletonization methods used, and by quantization errors. Even when imaged at the limits of light microscopy, single spines may span as few as three to 10 pixels, and neck diameters may be subvoxel resolution. The alternative to light microscopic approaches, electron microscopy, provides the greatest accuracy at these fine scales (Harris and Stevens, 1988; Harris et al., 1992; Harris and Kater, 1994) but would be prohibitively time consuming for reconstruction of entire dendritic trees or multicellular structures. Accurate recovery of fine neuronal geometry thus requires new skeletonization and analysis algorithms capable of subvoxel resolution at the light microscopic level. A primary goal of our

approach was the development of an automated system for digitization, 3D reconstruction and geometric analysis of detailed and accurate cellular and tissular morphology, capable of handling morphologic details on multiple scales.

EXPERIMENTAL PROCEDURES

General methods

Materials. The brains of six male Tg2576 mice older than 12 months, and six C57BL/6 wild type littermates, as well as four adult rats (300 g) were used for cell loading and 3D reconstruction. Custom-made transgenic mice expressing enhanced green fluorescent protein (eGFP) exclusively in neurons ($n=4$) were used for multineuronal networks reconstruction. All experimental protocols were conducted according to National Institutes of Health (NIH) guidelines for animal research and were approved by the Institutional Animal Care and Use Committee at Mount Sinai School of Medicine. Blocks from the prefrontal cortex (Brodmann's area 9) and from the hippocampus were obtained at autopsy after verification of consent from four patients with AD (78–85 years old, postmortem interval 3–8 h) through the Mount Sinai School of Medicine Alzheimer's Disease Research Center Brain Bank. All cases had a definite diagnosis of AD at neuropathological evaluation and had a clinical dementia rating score of at least 3. One hemisphere was fixed in 4% paraformaldehyde for 3–4 weeks and subsequently sampled for quantitative histopathology (Perl et al., 2000).

Tissue preparation. For single neuron imaging and multineuronal network reconstructions, animals were perfused transcardially with a mixture of 4% paraformaldehyde and 0.125% glutaraldehyde in phosphate buffer (pH 7.4) for 10 min. The brain was then carefully removed from the skull and immediately hemisected under a dissecting microscope. One hemisphere was sectioned at 200 μm on a Vibratome (Leica, Nussloch, Germany). In the case of Tg2576 mice, senile plaques were visualized in the thick section with 0.01% Thioflavine S after the cell loading procedure. Sections were coverslipped with Permafluor. This permits visualization of the loaded neurons in the context of amyloid plaque distribution in Tg2576 mice and reveals the possible effects of amyloid on the integrity of dendrites and spines. Human specimens were cut at 300 μm on a Vibratome and sections were stained with Thioflavine S for senile plaque visualization as above.

Autofluorescence quenching. The autofluorescence component of human sections due to lipofuscin can be quenched by posttreatment of the mounted sections in 1% Sudan Black B in 70% alcohol, rehydrated, and coverslipped (Romijn et al., 1999). This provides an efficient removal of bleed-through autofluorescence in case high levels of lipofuscin are present in human materials as well as in the oldest mice. Alternatively, autofluorescent components may be removed by imaging the labeled slices with the Zeiss LSM 510 META confocal laser-scanning microscope (CLSM, see Spectral Imaging and Linear Unmixing, following).

Cell loading with Lucifer Yellow. For intracellular injection, 200 μm-thick sections were incubated with 4,6-diamidino-2-phenylindole (DAPI; Sigma, St. Louis, MO, USA), a fluorescent nucleic acid stain, for at least 5 min, to reveal the cytoarchitecture under UV excitation. Then, sections were mounted on nitrocellulose filter paper, immersed in phosphate-buffered saline (pH 7.4), and visualized under epifluorescence. Using DAPI staining as a guide, neurons were impaled with sharp micropipettes, and loaded with 5% Lucifer Yellow (Molecular Probes, Eugene, OR, USA) in distilled H_2O under a direct current of 3–8 nA for 10–12 min, or until the dye had filled distal processes and no further loading was observed (Duan et al., 2002, 2003;

Page et al., 2002; Radley et al., 2005). Tissue slices were further mounted and coverslipped in Permafluor.

As with any technique to label or fill neurons *in vitro*, *in vivo*, or in postmortem materials, the issue of complete filling and ultimately of adequate recovery is a crucial one that needs to be carefully addressed. The authors are well aware that fine branches may not be as efficiently loaded as larger ones, and that some branches may be difficult to recover during imaging as a function of the depth within the thickness of the tissue. In addition some branches can be cut at the surface of the slice. Issues of abnormally cut dendrites can be addressed in a variety of ways (see for example Wu et al., 2004). It has been our practice to set relatively stringent criteria to retain neurons in a study. Entry into the analysis required that neurons: (1) lie within the layer or region of interest as defined by cytoarchitectural characteristics (which can be verified on adjacent materials stained with Cresyl Violet or by staining the slice with DAPI prior to performing cell loading); (2) exhibit complete filling of the dendritic tree, evidenced by well-defined endings; and (3) display intact primary, secondary, and tertiary branches (Hao et al., 2004; Wu et al., 2004; Radley et al., 2005). Cases where Lucifer Yellow is seen diffusing out of the cell body or dendrites usually indicate poor preservation of a cell's integrity or inadequate fixation of the specimen, and such cells would be rejected.

Microscopic imaging

Laser scanning microscopy (confocal and multiphoton). Tissue sections were examined using a BioRad Radiance 2000 multiphoton laser-scanning microscopy (MPLSM) system (Hercules, CA, USA) equipped with a Coherent Mira 900F Ti:sapphire laser (Santa Clara, CA, USA) and a Kr/Ar (488, 568 nm) laser. Tissue sections were also examined using a Zeiss LSM 510 META confocal laser scanning microscope (Jena, Germany) equipped with Ar (488 nm) and HeNe (543, 633 nm) lasers and/or a Leica TCS-SP (UV) confocal laser scanning microscope (Heidelberg, Germany), equipped with Ar (488 nm), Kr (568 nm), and HeNe (633 nm) lasers. For MPLSM, fluorescence from labeled neurons was imaged by using the Ti:sapphire laser (tuned to 860 nm for Lucifer Yellow) and a UplanApo/IR 60X (1.2 numerical aperture (n.a.), 0.25 mm working distance (WD)) water immersion objective lens. Serial optical sections (1024×1024 pixels; pixel dimensions $=0.2 \times 0.2$ μm) were collected through focus at 0.2 μm intervals. For higher resolution imaging, a UPlanApo $100 \times /1.35$ n.a. objective, (WD 0.1 mm) was used on the BioRad system in the multi-photon mode (i.e. with the Ti:sapphire laser) and/or the single-photon (confocal) mode (with the 488 nm line of the Kr/Ar laser). Single photon (confocal) imaging was also done on a Leica TCS-SP (UV) CLSM using a $100 \times$, 1.4 n.a. PlanApo lens and the 488 nm line of an Ar laser or on a Zeiss LSM 510 META confocal laser scanning using a $63 \times$, 1.4 n.a. PlanApo lens and the 488 nm line of an Ar laser. Serial optical sections (1024×1024 pixels with pixel dimensions $=0.18 \times 0.18$ μm [BioRad] or 0.1×0.1 μm [Zeiss or Leica]) were collected through focus at 0.1 μm intervals and correction for signal attenuation was performed as previously described (Rodriguez et al., 2003a). Collected data were saved to disk as BioRad pic files or stacks of TIFF images (Leica and Zeiss) and processed independently of each other before volume integration and reconstruction with the VIAS-NeuronStudio system.

To determine the effects of suboptimal image quality on the recovery of dendritic tree topology, confocal, multi-photon, and widefield imaging was also performed on tissue slices as the scan resolution (512×512–2048×2048), image capture bit depth (8, 12, 16 bit), objective magnification ($10 \times$, $20 \times$, $40 \times$, $63 \times$, $100 \times$) and n.a. (0.3–1.4) were varied. We have imaged Lucifer Yellow loaded neurons by CLSM over a 48-hour period without any noticeable photobleaching effects (Rodriguez et al., 2003a,b).
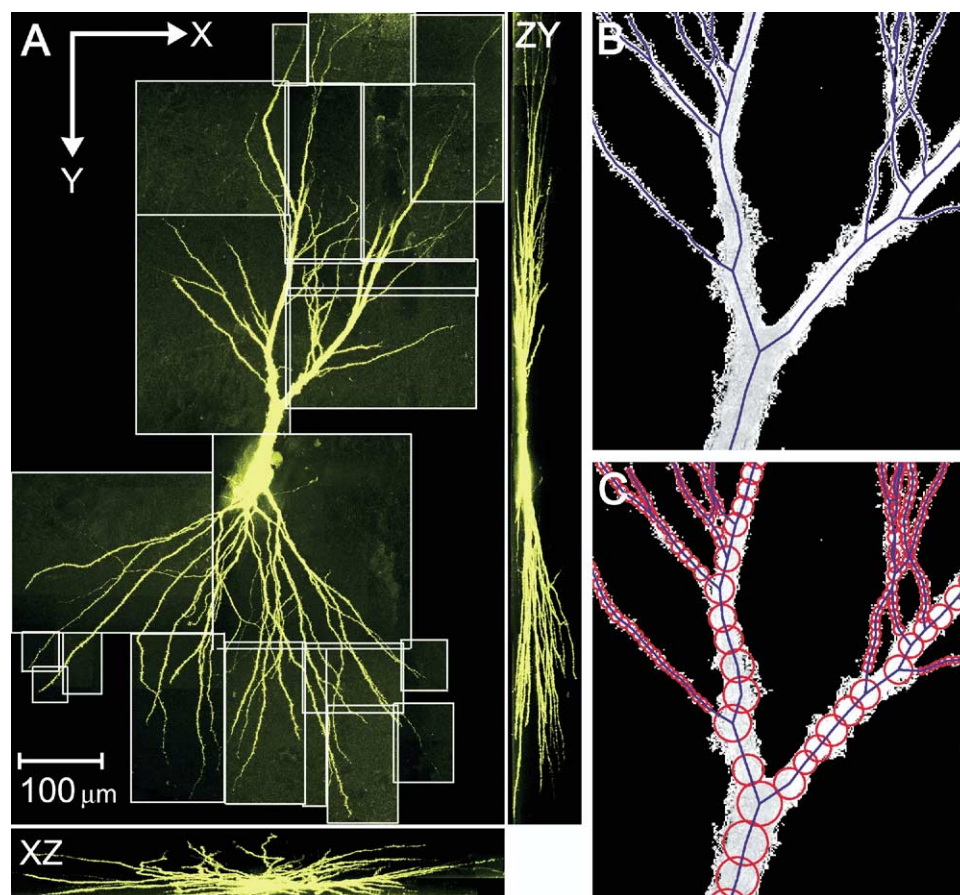
Fig. 1. Montage of CLSM tiled image stacks from CA3 pyramidal neuron, integrated with VIAS and skeletonized and digitized using NeuronStudio. (A) XY, XZ and ZY projections of the integrated volume. Individual subtiles selected from the original 12 image stacks and integrated with VIAS are outlined in green. (B) Skeletonized branches from the apical tree of the neuron in A. The medial axis is shown in blue, superimposed on the XY projection. (C) Skeleton with superimposed diameters (red circles) computed using the Rayburst sampling algorithm within NeuronStudio. (For interpretation of the references to colour in this figure legend, the reader is referred to the web version of this article.)

Widefield fluorescence microscopy. Tissue slices were examined on a Zeiss Axiovert 200 microscope and photographed with a Zeiss Axiocam MRm CCD camera using Axiovision software.

Multineuron networks. We used a custom-designed mouse model that expresses eGFP exclusively in neurons under an actin-nestin promoter. These mice express prominent eGFP fluorescence in the hippocampus and some regions of the prefrontal cortex. Tissue sections were imaged, tiled, deconvolved and reconstructed into integrated volumes with VIAS using the same imaging protocols as described above.

Spectral imaging and linear unmixing. Thioflavine S-labeled slides were imaged on a Zeiss LSM 510 META confocal laser scanning microscope equipped with a 63×, 1.4 n.a. oil immersion PlanApo objective lens. The META detector was used to generate spectral signatures (over a 240 nm range) for thioflavine S-labeled plaques and for lipofuscin autofluorescence in unlabeled sections. Lambda scanning was then done for thioflavine S-labeled sections and advanced linear unmixing (using the LSM 510 software) was used to separate the spectrally overlapping fluorescence of the thioflavine S-labeled senile plaques and the lipofuscin autofluorescence. The lipofuscin component of the image was removed, leaving the Thioflavine S components for surface analysis.

RESULTS

Digitization of individual neurons

To minimize subjective errors and optimize throughput, we have developed semi-automated tools for reconstruction and analysis of neuronal geometry from CLSM and MPLSM images (Rodriguez et al., 2003a). These techniques include noise filtering and deconvolution (Autodeblur, Autoquant Imaging, Troy, NY, USA), volume integration, automatic stack alignment and registration of adjacent tiles (Volume Integration and Alignment System (VIAS) system), surfacing and memory optimization for interactive visualization (Rodriguez et al., 2003a) and digitization in standard neuroanatomical formats.

Our VIAS software (http://www.mssm.edu/cnic/tools.html), integrates multiple stacks of tiled optical sections obtained from CLSM into a single volumetric dataset. VIAS uses projected volumes and hardware accelerated drawing to provide real-time interaction with the data. An autoalign tool corrects any small misalignments in the initial registration of adjacent images, ensuring that the tiling is accurately reassembled before the volume is integrated.
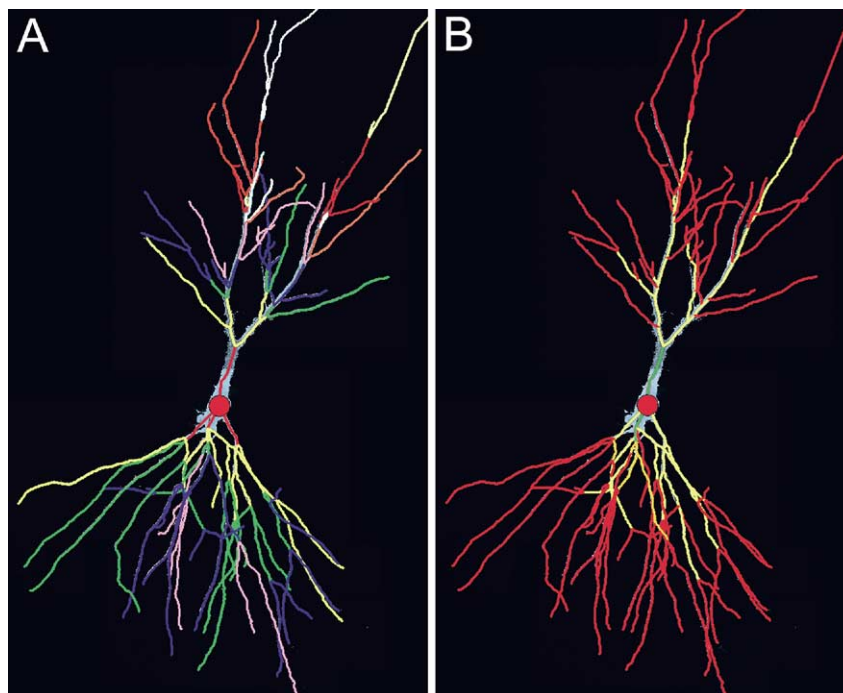
Fig. 2. Branch order analysis for reconstructed CA3 pyramidal neuron shown in Fig. 1. The extracted tree structure is shown superimposed on a projection of the integrated image stacks. The soma is indicated by the central red ball. (A) Centrifugal branch order analysis: lowest order (red) adjoins the soma and is incremented by one at each branch point as tree is traversed centrifugally (away from the soma). (B) Centripetal branch order analysis: lowest order (red) at branch tips is incremented by 1 as the tree is traversed centripetally (toward soma). See Tables 1 and 2 for color-coded explanation of branch orders, and summary statistics from 3D morphometric analysis.

Tree structure is then extracted from the integrated volume using an arborization and statistical analysis tool, Neuron-Studio (http://www.mssm.edu/cnic/tools.html), branching analysis performed, and the digitized file is output in a range of formats suitable for morphometric analysis, 3D display and standard compartment modeling software packages such as NEURON (Hines, 1994) and GENESIS (Bower and Beeman, 1998).

Extraction of tree topology using NeuronStudio

Deconvolved, filtered data are segmented using a thresholding algorithm (Rodriguez et al., 2003a,b). The entire volume is skeletonized to extract a medial axis that comprises a chain of voxels or nodes along the center of each branch (Fig. 1B), and accurate branch diameters are computed as a function of distance along the medial axis. Branch diameters are estimated at each point along the medial axis (Fig. 1C) using the new Rayburst sampling algorithm described below. We utilize a topology and ge-

ometry-preserving skeletonization method for volumetric objects (see Nikolaidis and Pitas, 2001, for review), with a custom modified iterative thinning algorithm (Lee et al., 1994; Borgefors et al., 1999; Tombre et al., 2000; Rodriguez et al., 2003a) to yield robust skeletons in an efficient manner. This is followed by loop removal, pruning to remove small barbs due to surface irregularities, tree smoothing and branch point repositioning (Tombre et al., 2000). These techniques are illustrated in Fig. 1, which shows an example of a CA3 hippocampal pyramidal neuron from a rat, imaged with a Radiance 2000 MP system (Bio-Rad). Images were digitized and fully reconstructed using NeuronStudio. Fig. 1A shows the three maximal projections onto XY, XZ and YZ planes of approximately 22 subtiles cropped using VIAS from the original 12 tiled and integrated CLSM image stacks over the soma and dendrites of the neuron. The relative planarity of CA3 neurons allows most of the dendritic tree to be captured within a 100 μm-thick section in the Z direction (XZ and YZ

Table 1. Centripetal branch order analysis of CA3 pyramidal neuron

Branch order	Branch count	Average length (μm)	SD length (μm)	Average diameter (μm)	SD diameter (μm)
1 (Red)	68	53.83	32.76	1.10	0.32
2 (Orange)	22	20.45	22.14	1.69	0.38
3 (Yellow)	8	50.26	27.85	2.94	1.09
4 (Green)	2	32.04	6.80	6.58	1.49

Table 2. Centrifugal branch order analysis of CA3 pyramidal neuron

Branch order	Branch count	Average length (μm)	SD length (μm)	Average diameter (μm)	SD diameter (μm)
1 (Red)	4	27.75	8.26	6.56	2.49
2 (Orange)	9	31.64	33.37	3.41	1.85
3 (Yellow)	14	31.38	25.61	2.37	1.42
4 (Green)	23	49.79	41.25	1.68	1.06
5 (Blue)	22	28.23	20.06	1.54	1.09
6 (Dark purple)	16	35.63	31.16	1.66	0.90
7 (Light purple)	14	43.00	28.27	1.52	0.88
8 (Flesh)	4	42.71	36.80	2.16	1.31
9 (White)	4	13.45	12.35	2.12	1.31
10 (Cyan)	4	12.54	16.66	2.36	0.72
11 (Brown)	6	26.58	18.31	1.52	0.75
12 (Khaki)	4	28.75	31.43	1.31	0.77
13 (Tomato)	4	59.72	31.85	1.15	0.39
14 (Grey)	2	73.42	9.41	0.71	0.04

projections, Fig. 1A). Fig. 1B shows a close-up view of the extracted medial axis (blue) following pruning and branch point correction steps. The threshold separating neuron from background is shown as a green outline. The estimated diameters at each node along the medial axis are shown as red circles superimposed on the skeleton and XY projection in Fig. 1C. Node density is a user-defined parameter, and can be increased up to one node per voxel for maximum accuracy, or reduced as in Fig. 1C, to optimize file size and computational efficiency. To maximize memory efficiency, VIAS uses two-dimensional (2D) projections rather than the volumetric data, and can be run on a standard desktop workstation. To align two large columns of dimensions 1024×1024×1000 pixels collected on our system for example, only 4.74 MB RAM are required to store the three planar projections of each of the two columns. The current beta version of NeuronStudio optimizes memory requirements by subsampling volumes to be skeletonized either once (reducing volumes eight-fold) or twice (reducing volumes 64-fold). This allows the entire reconstruction process to be run on a standard laboratory PC with ~2 GB RAM.

Analysis of branching statistics in individual neurons

Following digitization, automated branch order labeling and analysis can be performed in NeuronStudio, which generates summary statistics in tabular format for counts, lengths and diameters at each branch order (Fig. 2A, B; Tables 1, 2). Currently either *centripetal* (branch labels start from lowest order at tips, incrementing by one at branch points as tree is traversed centripetally, Fig. 2A) or *centrifugal* (lowest orders adjoin soma and increment by one at each branch point as tree is traversed outward, Fig. 2B), can be selected.

Branching analysis can be performed over the entire neuron, as indicated in Fig. 2, or separately over apical or basal subtrees. A selection mechanism will allow the user to pick individual structures of the model in a hierarchical manner ranging from low level objects such as vertices and edges up to entire sections, including loops and trees. This facilitates editing at multiple scales, and allows morphometry and statistical analyses to be performed on subtrees.

Development of new algorithms for anisotropic shape analysis and subvoxel metrics

The integer nature of digital images leads to quantization errors in standard skeletonization algorithms. Iterative thinning skeletonization methods can provide a distance in voxels from each tree node to the surface of the object. This distance is the D^6 metric, obtained by counting the number of voxels as they are removed in the minimal six-connected path from the surface to the medial axis. The D^6 metric is the 3D analog of the 'city block' distance in 2D (Borgefors, 1996). In existing skeletonization or vectorization algorithms for dendritic morphometry, the branch cross-section at any node is approximated as circular, with the D^6 metric providing the single diameter estimate (Koh et al., 2002; Al-Kofahi et al., 2003). The precision of this diameter estimate is limited to the physical size of the voxels. For small structures such as thin dendrites and spines, comprising only a few voxels even at maximal imaging resolution, the error can be significant if this measure is used directly (compare Fig. 3C and 3F). These quantization errors are illustrated in Fig. 3, which compares cross-sectional branch diameters estimated by the standard D^6 metric (left column, Fig. 3A–C) with diameters estimated by the Rayburst sampling algorithm (right column, Fig. 3D–F), described below. Fig. 3A and 3D shows a digitized branch, spanning only three to four pixels, in cross-section. The standard D^6 metric is indicated by the four blue vectors superimposed on the thresholded and segmented image in Fig. 3B. The length of the blue vectors (one pixel in Fig. 3B) determines the single branch diameter estimate, which is shown as a blue circle superimposed on the original branch cross-section in Fig. 3C. To minimize quantization error and evaluate more precisely
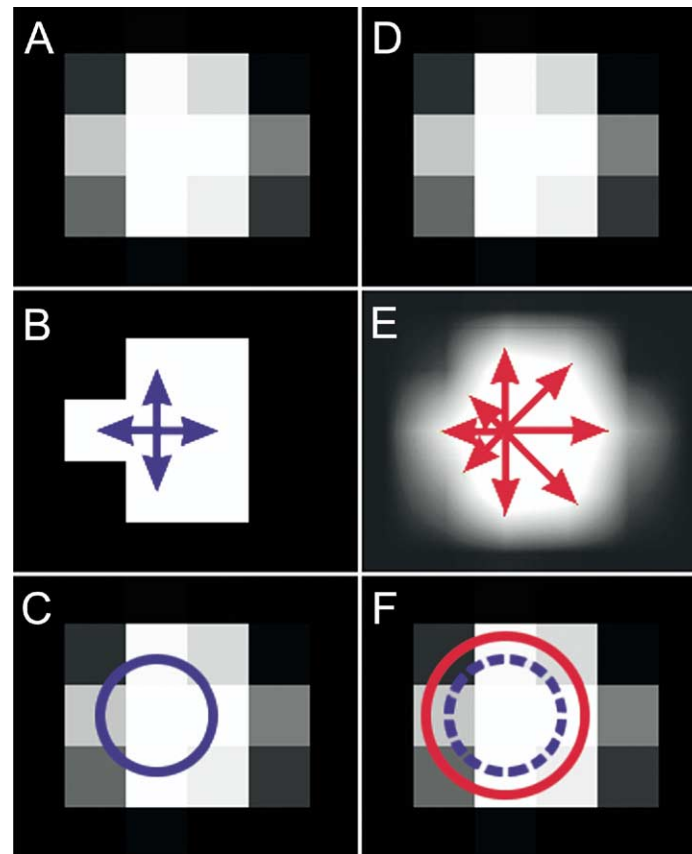
Fig. 3. Interpolation to correct quantization errors in diameter estimation that occur with standard D^6 metric. Left column: D^6 diameter estimation; Right column: Rayburst diameter estimation. (A, D) Thin branch cross-section. (B) Standard D^6 metric (blue vectors) counts voxels as they are sequentially removed during thinning. (C) Diameter estimated by D^6 metric. (E) Trilinear interpolated voxels with superimposed Rayburst vectors in red; (F) Comparison of diameters estimated by Rayburst (red) and D^6 metric (blue). (For interpretation of the references to colour in this figure legend, the reader is referred to the web version of this article.)

the geometry of the nodes, we introduce a new estimation technique, the Rayburst sampling algorithm that uses the original grayscale data rather than segmented images for precise, continuous radius estimation, and multidirectional radius sampling to more accurately represent non-circular branch cross-sections and non-spherical spine heads. These multidirectional Rayburst vectors are illustrated in red on the trilinear interpolated grayscale voxels in Fig. 3E. The resultant single branch diameter estimated by Rayburst is drawn as the red circle in Fig. 3F. This provides a better estimate of the actual branch diameter, and is substantially larger than the D^6-estimated diameter (dashed blue circle, Fig. 3F).

Rayburst sampling algorithm. The process of Rayburst sampling is defined as the simultaneous casting of rays in multiple directions, starting at a given point of origin inside a dataset. Each ray is allowed to grow from the origin until a given exit condition is reached. For the specific case of laser-scanning microscopy images, Rayburst is always run inside a lighted structure and the rays extended until the surface of the structure is reached. This can be determined as reaching a pre-specified threshold value or a given gradient. Rayburst sampling can be executed in one of two modes. In one-way mode each ray

starts at the origin and grows through the data until the exit condition is reached. The algorithm returns a set these lengths. In two-way mode, each ray starts at the origin and grows in forward and reverse directions until an exit condition is reached at each end. The algorithm returns a set of lengths each representing the sum of the forward and reverse distances.

For dendritic shape analysis, the algorithm precomputes an array of unit vectors, which sample the data in multiple directions from each node on the tree (the *sampling core*), from which an estimate of the node's geometry is computed (Fig. 4A, B). By varying the number of vectors, this information can be used to reconstruct 3D branches of arbitrarily irregular shapes. Standard morphometric and compartment modeling packages represent dendritic branches as generalized cylinders or truncated cones, i.e. as a chain of nodes with a single diameter at each node (Figs. 2C and 6C) which assumes a symmetric, circular dendritic cross-section. For compatibility with these packages while retaining maximum geometric information, we compute the diameter of an equivalent circular cross-section in the plane normal to the medial axis direction at each node (Fig. 3E, F), using the median lower band diameter (MLBD) described below.
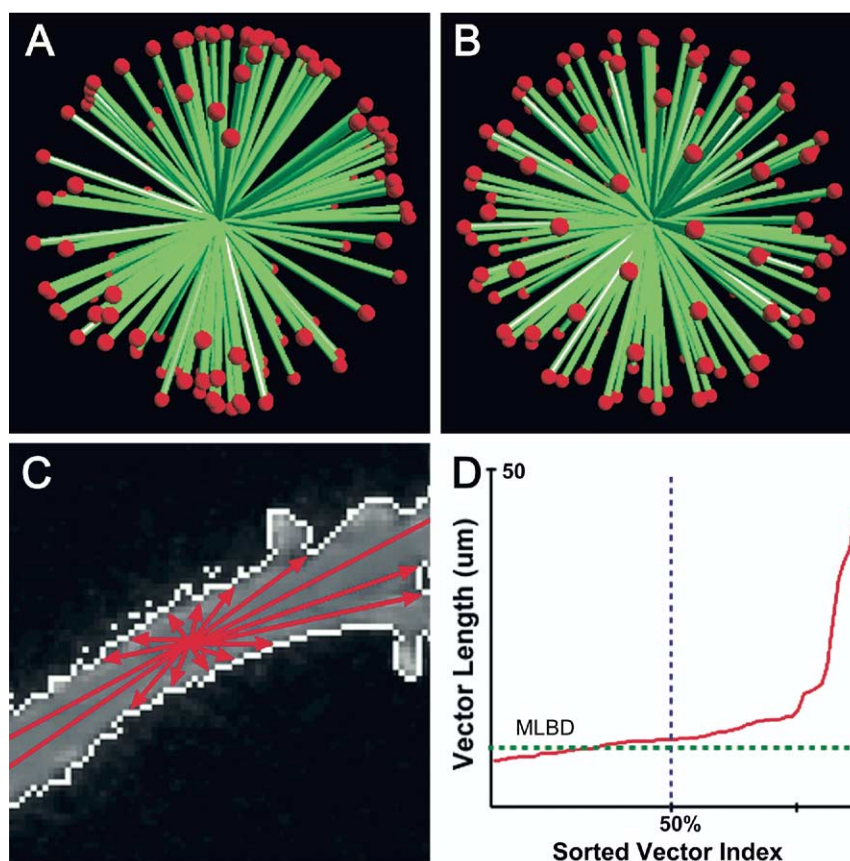
Fig. 4. Rayburst Sampling Core. (A) Random unit vectors before simulation. (B) After simulation, the sampling vectors are uniformly distributed over the unit sphere. (C) Distribution of Rayburst vectors inside thresholded dendrite. (D) Computation of MLBD from sorted Rayburst vectors.

Generating the sampling core. Accurate representation of each direction by the sampling core requires that its N vectors be uniformly spaced over the unit sphere (Thomson's Problem; Ashby and Brittin, 1986). Standard randomization schemes introduce systematic biases and for most N there is no simple analytic method of correcting this (Whyte, 1952; Conway and Sloane, 1993; Giraldo, 1997). Numerical methods, however, can provide a simple and effective approximation. In one-way Rayburst sampling, our algorithm uses a particle physics simulation in which a set of N randomly oriented unit vectors is generated (Fig. 4A), resulting in a random, nonuniform distribution of points on the sphere. The vectors are treated as charged particles constrained to move over the surface of the unit sphere. Each particle receives a repulsive force from every other particle, proportional to the inverse square of the distance between them. By iteratively displacing the particle in the direction of the resultant forces, we cause the particles to rearrange themselves (Fig. 4B). This system will tend to a stable, minimum energy configuration within approximately 40 iterations, where each particle is maximally separated from its closest neighbors (Rodriguez et al., 2003b). For two-way Rayburst sampling, each vector contributes two particles (positive and negative directions), resulting in a set of $2N$ points, distributed approximately uniformly on the sphere. Data are sampled at each node in

each of the $2N$ directions contained in the sampling core, to determine the distance along that direction from the node to the surface threshold. Quantization error due to the finite voxel representation is minimized by performing a trilinear interpolation (Hill, 1994) (Fig. 3E), which linearly interpolates points within a 3D box, given values at the vertices of the box.

Median lower band diameter (MLBD) estimation. Node diameters are estimated by computing the MLBD from the Rayburst samples. To compute the MLBD we take the set of $2N$ samples and add the corresponding pairs of opposite vectors, resulting in a set of N distances. We then sort the distances by size, define the lower band as the lower 50%, and use the distance at position $N/4$, representing the median of the lower band, to estimate the diameter. This provides good resistance to local irregularities in the surface and is invariant of the orientation of the segment (Rodriguez et al., 2003b). The estimate is particularly effective in and around branch points, where standard thinning and multidirectional concentric vectors confined to the plane tangent to the medial axis can overestimate actual branch diameters. A pseudocode description of the MLBD diameter estimation algorithm is given in Box 1.
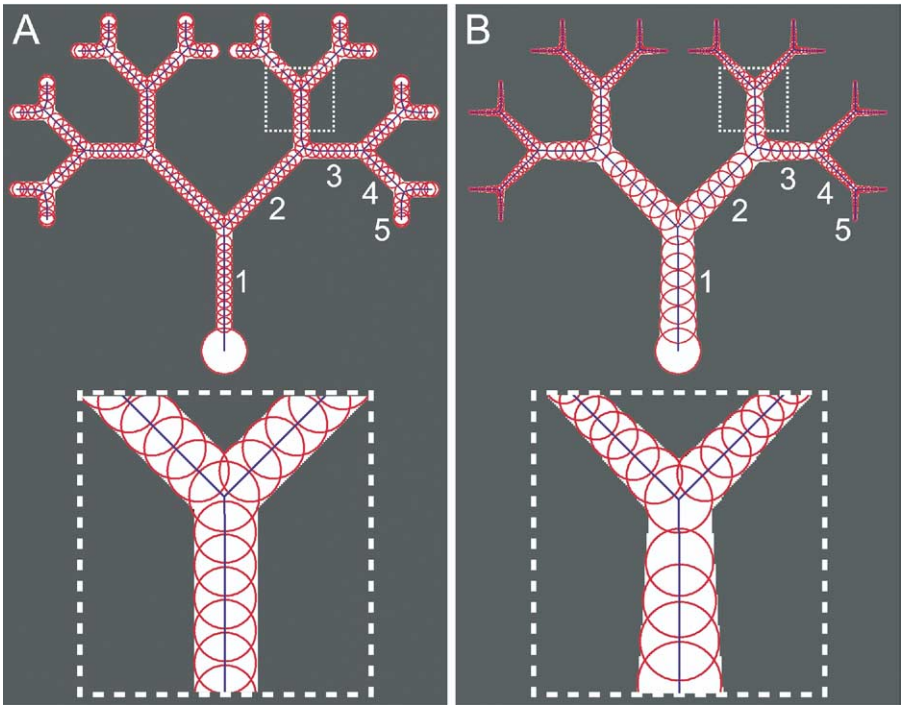
Fig. 5. Calibration of Rayburst MLBD diameter estimation using binary toy neurons with circular cross-sections. (A) Binary tree with constant branch diameters at each order. (B) Binary tree with continuously tapering branches. The numbers 1–5 indicate increasing branch orders, according to the centrifugal branch labeling system. The inset outlined by the white dashed box shows a close-up of skeleton and estimated diameters at branch orders 3 and 4 for each tree. The medial axis estimated by NeuronStudio is shown in blue. The diameters estimated by the Rayburst MLBD algorithm at points along each branch (red circles) closely approximate the actual diameter, regardless of taper. (For interpretation of the references to colour in this figure legend, the reader is referred to the web version of this article.)

Accuracy validation of Rayburst MLBD estimation. The accuracy of the skeletonization and Rayburst MLBD estimation algorithms was validated using 3D toy dendritic trees with known branch diameters and specified amounts of taper. Several different tree topologies were tested: binary trees with constant diameters at each branch order (Fig. 5A), binary trees with continuous taper within a single branch order (Fig. 5B), and nonbinary Mandelbrot-Vicsek fractal trees (Mandelbrot and Vicsek, 1989; Kabaso et al., 2003) with parent–child taper at branch points but no taper within a branch. The toy neurons were generated by first constructing a skeleton of specified dimensions as a list of conical frusta, defined by a point and radius at the start (x_1, y_1, z_1, r_1) and endpoints (x_2, y_2, z_2, r_2) of each branch. The branches were filled out by superimposing a series of spheres centered at each point along the medial axis of the branch. For the nontapering toy neurons, the radii of the spheres were constant at all branch orders. For the tapering toy neurons, the radii of consecutive spheres were linearly interpolated between r_1 and r_2 as the sphere center was moved in increments of one voxel along the direction of the medial axis.

Table 3. Statistics for accuracy validation of Rayburst MLBD diameter estimation

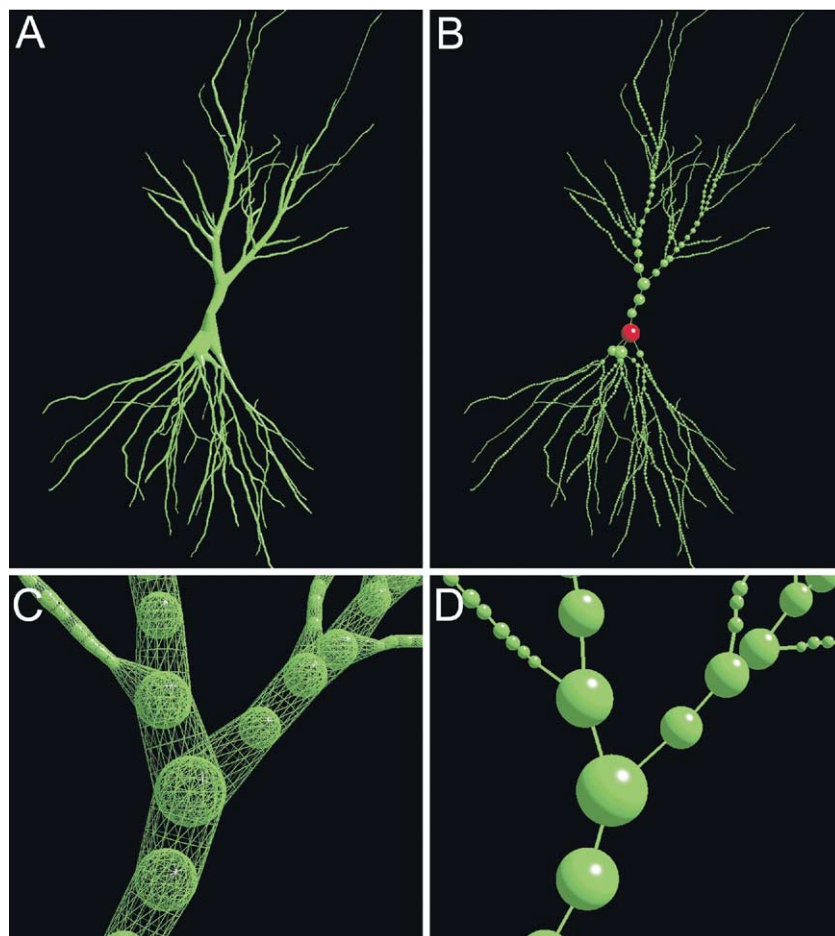| Branch order	Branch count	Actual average diameter (pixels)	Ave. diameter estimated by Rayburst (pixels)	Percent error
Nontapering binary toy neuron				
1	1	32.00	32.08	0.25
2	2	32.00	32.06	0.19
3	4	32.00	32.03	0.09
4	8	32.00	32.06	0.19
5	16	32.00	31.96	0.13
Tapering binary toy neuron				
1	1	73.00	72.90	0.14
2	2	55.16	55.19	0.05
3	4	39.00	38.97	0.09
4	8	22.62	22.57	0.20
5	16	10.00	9.97	0.34

Fig. 6. Fully digitized and reconstructed CA3 pyramidal neuron in cylindrical (A) and ball-and-stick (B) formats. The soma is represented as a red ball in B. (C) Zoomed view of apical dendritic tree in tapered cylindrical format. The close-up is shown as a wireframe to indicate the individual nodes and associated diameters, represented as spheres centered on each node. (D) The same zoomed view as in (C), in ball-and-stick format. (For interpretation of the references to colour in this figure legend, the reader is referred to the web version of this article.)

Fig. 5 shows the excellent fit of the estimated skeleton (blue) and superimposed spheres with diameters computed by the MLBD algorithm (red circles) for the binary tree without taper (Fig. 5A) and with continuous taper within branches (Fig. 5B). Table 3 shows the results of the branch order analysis and percent errors computed between the actual branch diameters, and the average diameters estimated by the Rayburst MLBD algorithm at each order, for the two toy neurons shown in Fig. 5. These statistics were calculated as follows: for every branch at every order, the actual diameter at the start and end of the branch was recorded manually by measuring it from a 2D projection using a simple ruler tool in Adobe Photoshop (Adobe Systems, Inc.), and compared with the diameter estimated by the Rayburst MLBD algorithm at the same point. The average diameter for every branch was computed as the mean of the start and end values. The average diameters for each branch order, both actual (Table 3, column 3) and Rayburst MLBD estimates (Table 3, column 4), were then calculated as the mean of the average diameters of all branches at that order. Finally the difference between the manual and automated methods was expressed as a percentage error (Table 3, column 5). For the binary toy

neurons shown in Fig. 5, the Rayburst MLBD algorithm correctly estimated the actual branch diameters to within 0.3%

Box 1. Pseudocode for Rayburst MLBD estimation

Let the model be represented as a set of vertices, where each vertex V is defined by its position $[x,y,z]$ in R^3 and its diameter, d. Then d can be estimated as the MLBD as follows:

N=number of directions in sampling core

```
for each vertex position [x,y,z]
  {
    for each direction Dᵢ in sampling core
      {
      R1=Dᵢ cast from [x,y,z] to surface
      d1=length of R1
      R2=−Dᵢ cast from [x,y,z] to surface
      d2=length of R2
      samples[i]=d1+d2
      }
    Sort(samples)
    d=samples[N/4]
  }
```
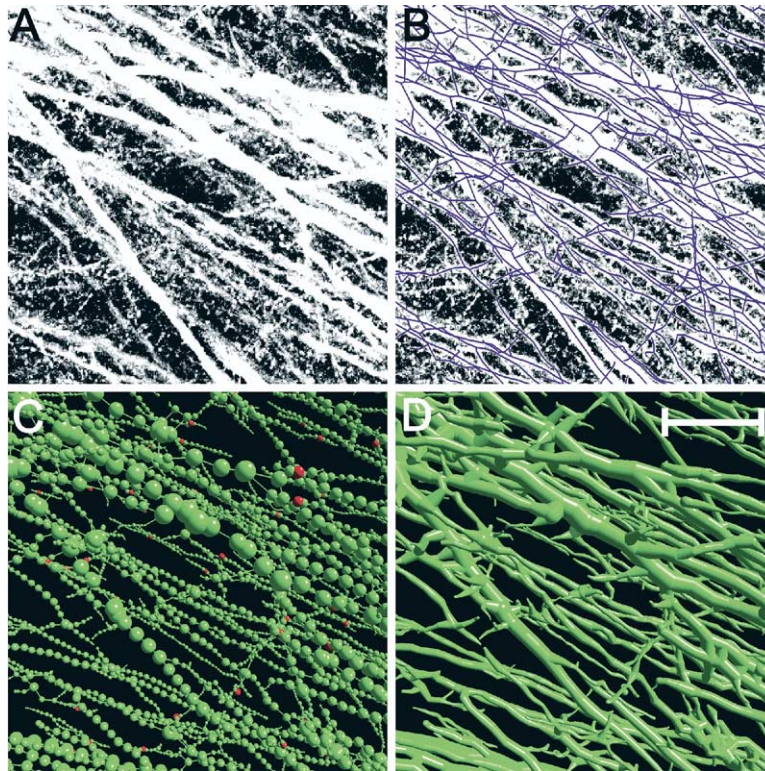

Fig. 7. Extraction of 3D skeleton and mass distribution from multineuron network in hippocampus of an eGFP mouse. (A) Projection of CLSM images from hippocampal field of eGFP mouse. (B) Projection as in (A), with superimposed skeleton. (C) Skeletonized dendritic field in ball-and-stick format. (D) Generalized cylinder representation of digitized dendritic field.

accuracy. The maximum percentage error was only slightly larger for the Mandelbrot-Vicsek toy neuron, at 0.45%.

Current work is extending the Rayburst algorithm to allow for anisotropic branch cross-sections by estimating distances from the medial axis to the branch surface in multiple radial directions. This will permit noncircular branch cross-sections to be more accurately represented in the digitized tree structure.

Output file format. For maximal compatibility with existing morphometry and compartment modeling packages, digitized data can be output in several standard neuroanatomical formats. The default format is .swc format (Cannon et al., 1998), where each node is represented as a single line in a text file: [n T x y z R P]. In this format, n is an integer label that identifies the current point and increments by 1 from one line to the next. The variable T is an integer representing the type of neuronal segment, such as soma, axon, apical dendrite, basal dendrite. The sequence [x,y,z] gives the Cartesian coordinates of each node, and R is the radius at that node. Connectivity is represented by the point P, indicating the *parent* of the current point, when traversing the tree centrifugally, i.e. away from the soma. Some application-specific output file formats are also supported, including .hoc format for importing into compartmental modeling software such as NEURON (Hines, 1994).

The final digitized and reconstructed CA3 pyramidal neuron of Figs. 1 and 2 is shown in Fig. 6, represented either in generalized cylinder format (Fig. 6A, C) or as a 3D skeleton with superimposed balls of the appropriate diameter at each vertex (Fig. 6B, D). Zoomed-in views of each representation, generalized cylinders in Fig. 6C; skeleton with 3D balls in Fig. 6D, demonstrate adequate recovery of branching structure at a moderately coarse level of digitization.

The original 12 image stacks, each 0.5 GB, represent 6 GB of raw data. Following subsectioning and registration with VIAS (green subtitles in Fig. 1A), the integrated volume is reduced to 1 GB, from which the extracted tree structure in generalized cylinder format comprises only 316 kB, depending on the fineness of discretization selected by the user. At the highest resolution, one node per voxel in the medial axis is possible; at lower resolutions redundant nodes can be culled whenever (i) curvature of the medial axis is low; (ii) between branch points, and (iii) branch diameters are relatively constant. At the moderately coarse level of discretization shown in Fig. 6, data compression from the original raw data to the digitized model is 18,615:1; compression from the integrated volume to the digitized model is 3318:1.

Digitization and analysis of multineuron networks in 3D

Analysis of global spatial complexity of biological network structures has to date been restricted to blood vessel networks (Gazit et al., 1997; Abdul-Karim et al., 2003; Jain, 2003; Fridman et al., 2004) and canal networks in bone structures (Cooper et al., 2003). Few
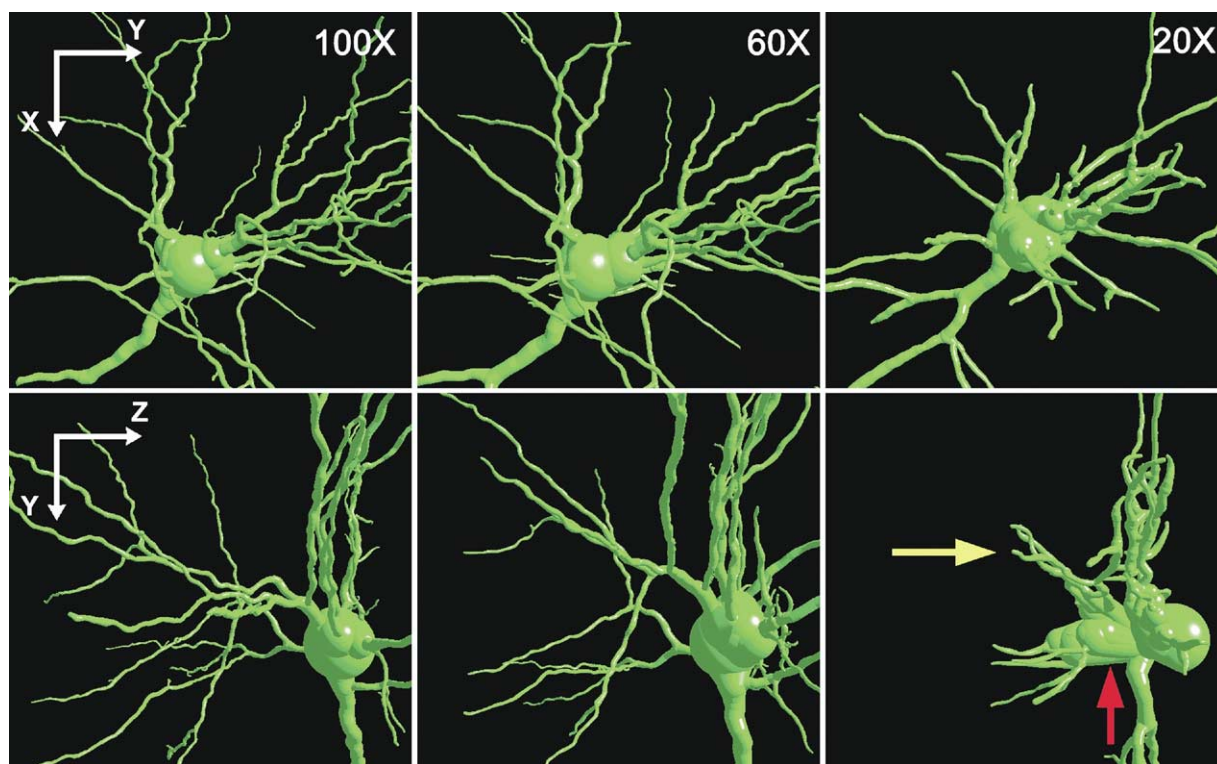
Fig. 8. Sequence of 3D models comparing the extracted trees from the same tissue section, imaged using CLSM, viewed in XY orientation (top row) and YZ (bottom row). The three columns compare the effects of different values of objective magnifications and n.a.: 100×, 1.35 n.a. (left column); 60×, 1.4 n.a. (center) and 20×, 0.4 n.a. (right column), using 8-bit grayscale depth and a constant field size of 1024×1024 pixels. Note that while the XY-projection of the reconstructed models adequately represents tree topology, loss of resolution in the Z direction is the limiting factor for accurate recovery of 3D tree topology in the 20× model (red and yellow arrows). (For interpretation of the references to colour in this figure legend, the reader is referred to the web version of this article.)

attempts have been made to quantify the structure and connectivity of spatially complex neural networks in 3D. In the normal brain, global patterns of network connectivity and the resulting columnar and microcolumnar structures (Mountcastle, 1978, 1997; Braitenberg and Braitenberg, 1979; Rockland and Ichinohe, 2004) are central elements in the functional organization of cortex, yet to date our understanding of these structures has been derived from 2D measurements. The functional repercussions of space-occupying lesions such as amyloid plaques in AD and compromised microvasculature in a number of pathological conditions on the normal network structure also remain to be determined. This is primarily because of the inability of existing imaging and reconstruction techniques to represent entire regions of cortical tissue in 3D, at the dendritic level of resolution.
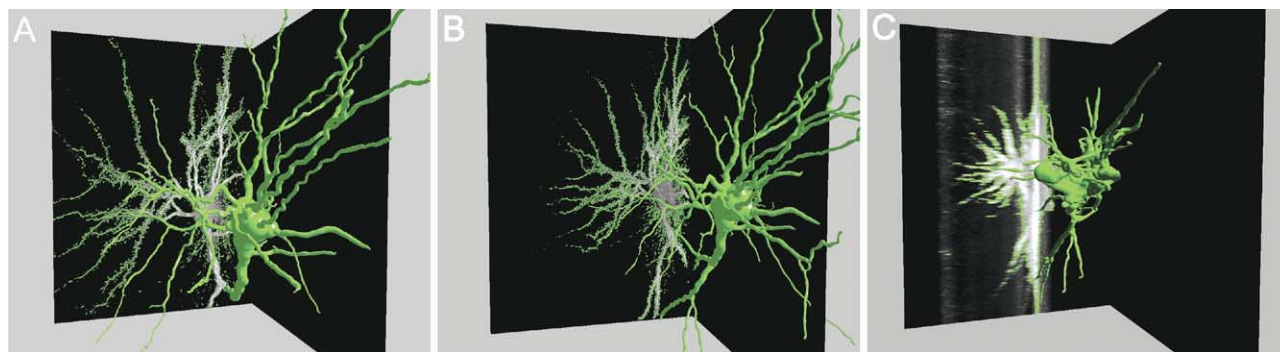

Fig. 9. Model shown in 3D with YZ projections cast onto the back wall. Effects of reduction in magnification from 100× to 60× to 20×. Models are shown in 3D in the foreground, side projections with overlaid threshold (green border) in the background. (A) Full recovery of dendritic structure with little or no breakage at 100×. (B) Excellent recovery of dendritic structure, minimal breakage, but reduction in dendritic length at lower depths at 60×. (C) Highly inaccurate structure at 20×. Only the largest dendritic segments can be recovered. Artifactual segments and loops especially near the soma prohibit true analysis of the model. To assist visualization, models are not shown to scale. (For interpretation of the references to colour in this figure legend, the reader is referred to the web version of this article.)
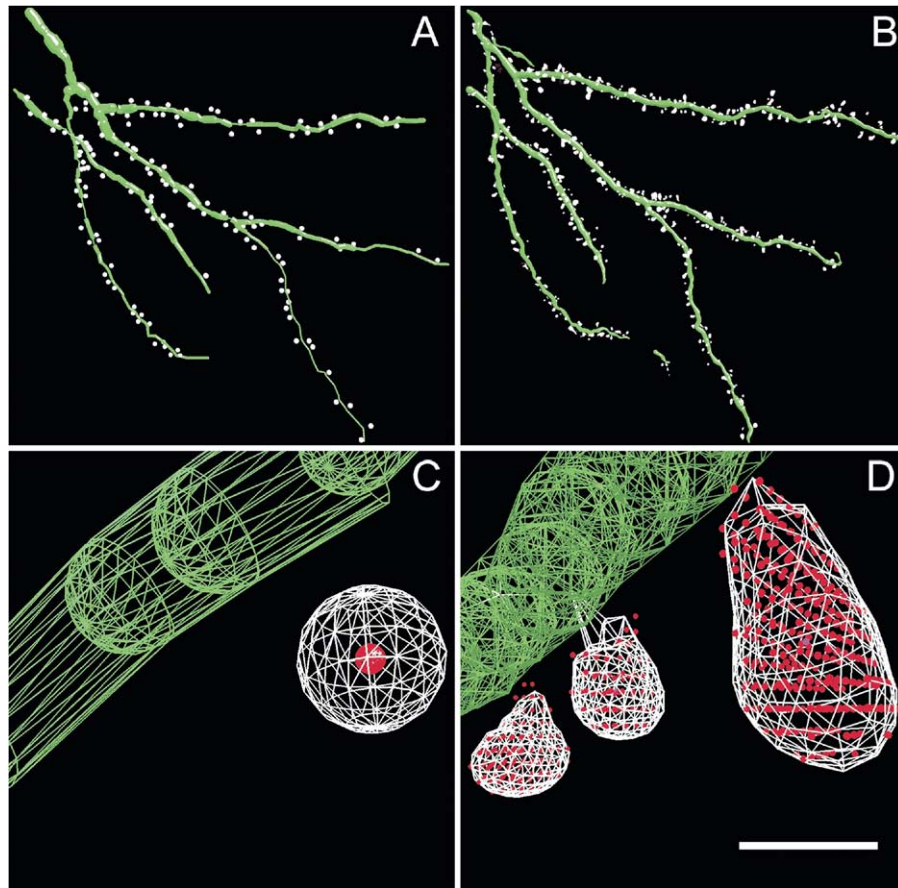
Fig. 10. Comparison of spine numbers and shapes detected using manual tracing from tissue blocks (A, C), and using automated spine detection with NeuronStudio (B, D). (A) A total of 140 spines were detected using manual tracing. (B) A total of 441 spines were detected from confocal laser scanning microscopy images. (C) Zoomed view of a branch segment from A, where a single spine was detected manually. The spine is indicated as a red sphere, centered at the point of detection. The white sphere surrounding the spine is for visualization purposes only; no information on spine shape or size can be recorded in the manual tracing. (D) Zoomed in view of the same branch segment as in C, taken from the automated reconstruction in B. Three spines were detected using the automated clustering routine. These spine clusters are represented by the red voxels comprising each cluster, with superimposed white surface mesh determined by applying one-way Rayburst at the center of mass of each cluster. Scale bar=30 μm in A, B and 0.5 μm in C, D. (For interpretation of the references to colour in this figure legend, the reader is referred to the web version of this article.)

A recent attempt to reconstruct 'neuronal forests' in 3D from thinly sectioned Golgi-stained tissue blocks by McCormick and colleagues (McCormick, 1999; Burton et al., 2001) used brightfield microscopy and a novel knife-edge scanner. The network connectivity recovered by this technique, however, is restricted to the variable fraction of neurons stained by the Golgi technique and the maximum resolution obtainable.

To provide a better representation of the true network structure in normal and pathologic tissue, we are using a transgenic mouse model expressing the eGFP gene under the control of an actin-nestin promoter and cre-loxP system to visualize the spatial patterns of complete dendritic arbors in multineuron networks including most of hippocampal, and some neocortical neurons. These eGFP-positive neurons were imaged using MPLSM on 200 μm fixed coronal slices with a long WD lens (60×) (Fig. 7). Following computer-assisted 3D reconstruction including deconvolution and volume integration, the global structure of the network is clearly visible, as are irregularities in spatial structure (Fig. 7). The data were skeletonized using

NeuronStudio to extract a medial axis for each branch (Fig. 7B). In order to recover the mass of individual dendrites, the Rayburst algorithm was used to estimate the diameter of each branch, at each node along the skeletonized branches. Fig. 7C shows the reconstructed skeleton with superimposed diameters in 'ball and stick' format, and Fig. 7D shows the reconstructed 'generalized cylindrical' representation of the network. This 3D digital representation along each node permits measurements not only of the fractal characteristics of the branching patterns per se, as is usually performed in fractal studies of tumor vasculature in studies of cancer (Gazit et al., 1997; Jain, 2003), but also of the degree of irregularity in branch diameters, and hence in global mass distribution (Henry et al., 2002).

Effects of suboptimal image quality on recovery of dendritic tree topology

High-resolution confocal and multiphoton laser scanning microscopy and/or high n.a. objective lenses are not universally available in all laboratories. For applications
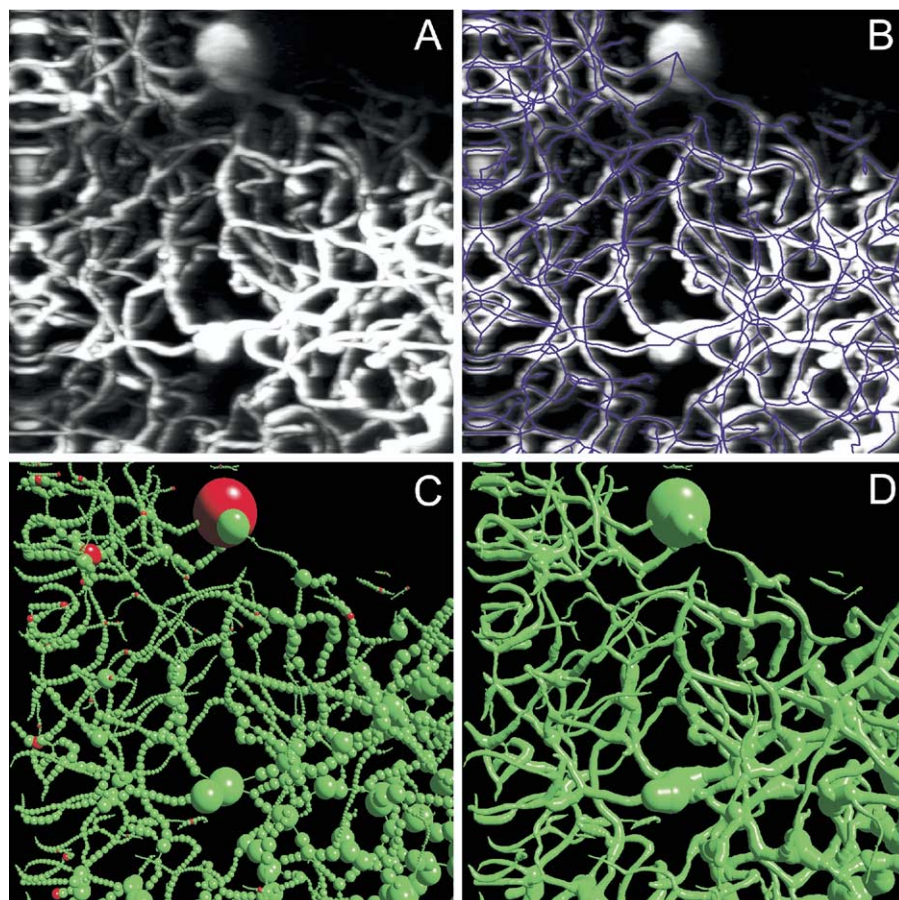
Fig. 11. Extraction of skeleton and mass distribution of a portion of a capillary bed in the living rat barrel cortex. The animal was anesthetized, a skull flap was made, the dura mater removed, and the underlying cortex viewed through a microscope coverslip with a 20× objective (n.a. 0.9; Olympus, Melville, NY, USA) on a custom-made multiphoton laser scanning microscope. The light source was a Chameleon tunable laser (Coherent). Fluorescein, introduced via the femoral vein, was excited at 810 nm. (A) Projection of MPLSM images. (B) Projection as in A, with superimposed skeleton shown in blue. (C) Ball-and-stick representation of vascular network showing superimposed diameters. (D) Generalized cylinder representation of vascular network. The darker areas result from the presence of large pial vessels casting a shadow on the field. (For interpretation of the references to colour in this figure legend, the reader is referred to the web version of this article.)

whose aim is to capture gross tree topology in large numbers of neurons, imaging the entire dendritic arbor at low to medium resolution may suffice. To assess the minimum image quality necessary to recover accurate tree geometry suitable for compartment modeling, we are conducting a comprehensive analysis of the effects of noise, image resolution (optical and scan resolution), bit depth, imaging platform (CLSM, MPLSM and epifluorescence) on the accuracy of the extracted arbors. Here we report on the effects of objective lens magnification, n.a. and bit depth for CLSM images. Pyramidal neurons from C57BL/6 mice were loaded with Lucifer Yellow and imaged using CLSM over a range of magnifications (using 100× to 10× objective lenses), optical resolutions (as related to values of n.a. ranging from 1.4–0.3 n.a.), bit depths (16, 12 and eight-bit) and pixel dimensions (i.e. image capture resolution). Images were deconvolved and skeletonized to extract dendritic arbors, which varied in overall size and accuracy depending upon the imaging mode and parameters. Fig. 8 compares 3D models of the extracted arbors from an initial analysis of the CLSM data from the same pyramidal neu-

ron, imaged with different values of objective magnification and n.a.: 100×, 1.35 n.a. (left column); 60×, 1.4 n.a. (center) and 20×, 0.4 n.a. (right column).

The reconstructions varied in quality and extent, as the bit depth was reduced from 16-bit to 8-bit. Confocal imaging at 100× with 16-bit grayscale depth and voxels of $0.1 \times 0.1 \times 0.1$ μm gave the optimal result with >90% of the tree recovered without breakages. Reductions in bit depth from 16 to 8 bits affected the extracted tree only minimally (Fig. 8, left column), while reductions in objective magnification and n.a. from 60× (1.4 n.a., Fig. 8 center) to 20× (0.4 n.a., Fig. 8, right column) caused the greatest reductions in completeness of the extracted trees. In images collected using a 20× (0.4 n.a.) objective, dendritic lengths were truncated (yellow arrow, Fig. 8), and loss of resolution along the z axis limited reconstruction of somatic shape (red arrows, Fig. 8). Fig. 9 highlights the loss of dendritic length and resolution along the optic axis as objective lens magnification is reduced from 100× (Fig. 9A) to 60× (Fig. 9B) to 20× (Fig. 9C), by showing the reconstructed model in 3D with YZ projections from the deconvolved image

stacks cast as shadows onto the back wall. In Fig. 9C, two independent factors prevent accurate recovery of tree topology: (1) the loss of XY resolution primarily truncates the lengths of dendritic branches; (2) the loss of resolution along the optic axis at 20× creates artifactual loops and smearing, particularly close to the soma, resulting in a coarse model lacking fine details. It will be important to perform further statistical analyses of the imaging parameters at which the branch lengths, branch diameters and detectability of spines in the reconstructed tree become significantly different from the standard (imaged by confocal microscopy with a 100× (1.4 n.a.) objective lens, a bit depth of 16, pixel dimensions of 0.1×0.1 μm and z-steps of 0.1 μm). This will include the assessment of the effect of changes in objective lens resolution that are independent of magnification (i.e. 40×, 0.6 n.a. vs. 40×, 1.3 n.a.).

We conclude from these initial results that a minimum of 60× magnification (1.4 n.a.) with 8-bit grayscale range and voxel sizes of approx. 0.2×0.2×0.2 μm with a field size of 1024×1024 would be required for adequate automated reconstruction of the entire tree, without significant manual intervention. Nonetheless, even using a 40× (0.6 n.a.) objective lens with 8-bit grayscale range (not shown in Fig. 8), we were able to obtain a fair representation of the tree, provided that disconnected dendrites were visually reconnected during a final manual tree-editing phase.

Emerging applications

Spine analysis. Spine shape analysis is a major emerging application of the Rayburst sampling algorithm. The multidirectional radial measures returned by the Rayburst sampling core are very well suited to analysis of the wide range of normal spine shapes, as well as the irregular geometries that occur in pathologic conditions and brain aging. Preliminary work has demonstrated that manual counting of spines from tissue slabs in epifluorescence microscopy, on a live computer display, significantly underestimates spine numbers (Duan et al., 2002, 2003; see also Fig. 10). In Fig. 10A, the branching structure has been manually traced and the spines counted from the computer display of an epifluorescence microscope using NeuroLucida. The dendrites were followed and traced at 100×, and spines were marked as they appeared in best focus on the display. This approach has severe limitations in that not all spines are visible especially deep into the sections and close to the dendrite where the scattering properties of the tissue prevent spines directly above or below the dendrite from being resolved, resulting in significant underestimates of spine numbers (see also Fig. 3 of Rodriguez et al., 2003a) These manual spine counts are compared with automated spine analysis from a single confocal image stack using NeuronStudio (Fig. 10B).

To avoid the problems inherent in manual tracing, we are developing automated spine detection and analysis routines based on the Rayburst sampling technique. Fig. 10B, D shows results of a preliminary analysis using these routines, applied to the same tissue block as was manually traced in Figs. 10A, C. Spines were detected by creating clusters of voxels that pass a set of user-defined criteria

depending upon the species and neuron type. These criteria include intensity, minimum and maximum distances from the closest branch and bounds on the allowable volume. The clusters were then analyzed to determine total volume, surface area and attachment point to the closest branch. One-way Rayburst sampling was applied at the center of mass of each cluster, and lengths of each ray to the surface threshold were determined. A polygonal mesh connecting the ends of the rays creates a surface manifold for the spine, approximating arbitrarily irregular shapes with greater precision as the number of rays in the sampling core is increased. Spine volume is found by summing the volume of the tetrahedral formed by each triangle in the mesh and the center of mass of the cluster. Spine surface area can simply be found by summing the surface area of each triangle.

A total of 140 spines were detected in the manual counting procedure (Fig. 10A), compared with 441 detected in the automated count (Fig. 10B). One limitation of automated detection techniques is that the higher number of potential spines identified may include false positives, i.e. small clusters of autofluorescent material that fall within the acceptance criteria and are otherwise undistinguishable from spines. Ongoing work is focused on refining the criteria for classification of clusters as potential spines to minimize these false positives. Examination in 3D of the models of Fig. 10A, B however, demonstrated that many of the potential spines identified by the automated algorithm and missed by the manual procedure were small clusters located either immediately above or below a dendrite, and hence difficult to distinguish visually by focusing down through the tissue slice.

Perhaps the major advantage of the automated spine analysis technique is its ability to represent spine morphology. Fig. 10C, D compares spine morphologies identified by the two techniques. Fig. 10C shows a close-up view of a manually traced dendritic branch with a single detected spine. The spine and branch have been rendered in 3D from the original NeuroLucida file, using our visualization program, NeuroGL (http://www.mssm.edu/cnic/tools.html). The red center shows the actual point surrounded by a white sphere of arbitrary size, drawn around the point for visualization purposes only. Fig. 10D shows a close-up view of the same dendritic branch and spines detected by the NeuronStudio/Rayburst system. The red points are the voxels comprising the spine cluster. The white polygon mesh is the surface manifold of the spine as determined by application of the one-way Rayburst at the center of mass of the cluster. Not only are two additional potential spines found using the automated technique, but a fairly good representation of spine morphology is provided by surfacing the detected clusters (Fig. 10D). In future studies, both the numbers of detected spines, and their 3D morphologies will be validated using computer-generated models of spiny dendrites with a range of spine types of specified dimensions.

Quantification of 3D spatial complexity in vascular networks in vivo. Abnormal vasculature is a hallmark of many human diseases (Carmeliet, 2003), and of solid

tumor or lesion development, in particular (Jain, 2002; Jain et al., 2002). Blood vessels in tumors do not follow the hierarchic branching pattern of most normal vascular networks—the normal equilibrium between vascular growth and cellular demands in tumors results in avascular, hypoxic voids of multiple sizes. When quantified with fractal measures such as fractal dimension, minimum path length (a measure of tortuosity) and lacunarity, the size and number of such voids correspond to invasion percolation, a stochastic process in which a network expands around randomly distributed obstacles (Baish and Jain, 2000). Such approaches have revealed the extent of abnormality in tumor vascular networks, the effect on nutrient and drug delivery and the process of vessel normalization during different therapies (Gazit et al., 1995, 1997; Baish and Jain, 2000). Significantly, tumor and vascular growth can also be simulated with statistical growth models, providing insights into tumor morphology and function that are important for understanding the transport of nutrients in tumors, and for the design and delivery of blood-borne treatments. Furthermore, the functional integrity of the brain microvascular network is crucial for the maintenance of energy metabolism and furnishing oxygen and nutrients to the brain parenchyma (Magistretti and Pellerin, 1999; Magistretti, 2000). Considering that the microvascular network can be severely altered in neurodegenerative disorders (Buée et al., 1994; Bailey et al., 2004), it becomes important to assess quantitatively and dynamically potential disease- or aging-related alterations in the brain microvascular bed in animal models. Recent technology permits *in vitro* and *in vivo* approaches to these issues (Nedergaard et al., 2003). Although relatively difficult, live imaging of the microvasculature following injection of a fluorescent dye in the peripheral circulation is feasible. We have recently applied our imaging and 3D reconstruction protocols successfully to such microvascular networks (Fig. 11). This will make it possible to observe and quantify changes in blood vessels and blood flow dynamics in physiological conditions as well as in models of human diseases.

Imaging, digitization, and 3D analysis of space-occupying histopathologic lesions. To date, global analyses of tumor surface characteristics have been performed only in 2D. In particular, analysis of the spatial complexity of these structures has been performed either on 2D projections, or using skeletonized medial axes without accounting for the mass distribution. In recent work, 2D projections of tumor surfaces (Lefebvre et al., 1995; Pohlman et al., 1996; Einstein and Gil, 1998; Einstein et al., 1998) were segmented, then analyzed using planar box-counting, box-gliding or similar methods. Inferences of fractal dimensions and growth mechanisms based on such 2D data are not accurate representations of the true 3D spatial complexity, however (Sander et al., 1983; Witten and Sander, 1983). For example, diffusion-limited aggregation (DLA; Witten and Sander, 1981) is a standard model in statistical physics of growth processes in which the aggregation of particles into clusters is dominated by diffusion. DLA in 2D results in clusters with a fractal dimension of $D=1.7$, whereas clusters from the same mech-

anism but grown in 3D have a fractal dimension of $D=2.5$. Hence a measurement of $D=1.7$ for a thin 2D projection is not indicative of DLA-like growth. In order to test hypotheses about growth mechanisms, new algorithms that permit accurate analysis of complex cellular structures in 3D are essential. Significantly, unlike the existing 2D tools, 3D measures of surface texture in lesions such as amyloid plaque or tumor formation will be capable of distinguishing between potential normal and pathologic *growth mechanisms* (Batchelor et al., 1998a,b), and may be useful for future modeling studies in which the effects of the disease process can be simulated.

In preliminary studies we have imaged samples of amyloid plaques from aged humans with AD and Tg2576 mouse. The Thioflavine S-labeled slides were imaged on a Zeiss LSM 510 META CLSM in the lambda scanning mode to generate independent spectral signatures (i.e. emission intensity profiles) over a 240 nm range for the fluorescence signal from Thioflavine S-labeled plaques in Tg2576 mice and for lipofuscin autofluorescence in unlabeled human AD brain sections. Lambda scanning was then done for Thioflavine S-labeled plaques in lipofuscin containing human AD brain sections and linear unmixing (using the LSM 510 software) was used to separate the spectrally overlapping fluorescence of the Thioflavine S-labeled senile plaques from the lipofuscin autofluorescence. The lipofuscin component of the image was removed, leaving the Thioflavine S components for surface analysis (Fig. 12A–C). Following imaging and linear unmixing, the extracted plaque data were deconvolved, thresholded and digitized into 3D coordinates with origin at the center of mass of the plaque. Using NeuronStudio, a range of different thresholds was determined visually (Fig. 12D, E). As shown in Fig. 12G, H, the computed 3D surface depends critically upon the "tightness" of the threshold. A preliminary analysis of surface roughness also indicates a strong dependence of computed surface roughness on the chosen threshold (Batchelor et al., 1998a; Westpfahl et al., 1999). For finer estimation of surface characteristics, the Rayburst algorithm with subvoxel metrics described above can be used to avoid quantization errors that can artifactually alter the estimated surface roughness.

Not only is the morphology of space-occupying lesions such as amyloid plaques of interest, but its effects on local neuronal morphology and function remain to be characterized. Fig. 12F, I shows the effect of local amyloid beta accumulations on dendritic and spine morphology in the frontal cortex of a 14 month-old Tg2576 mouse. We observed that as amyloid deposits increase in density in this model substantial alteration in the fine structure of dendrites are revealed. Dendrites in the vicinity of a plaque are displaced and must take longer, more tortuous routes to circumvent it (Fig. 12F), while dendrites that traverse a plaque may suffer local spine loss or distortion of spine geometry (Fig. 12I). These observations are comparable to previous findings in other AD mouse models (Knowles et al., 1999; Le et al., 2001; Tsai et al., 2004). However, until precise 3D models of these geometric distortions are produced, investigations of their functional effects (e.g. by compartmental modeling of the resulting changes in neuronal firing patterns) will be limited by the accuracy of the reconstructions.
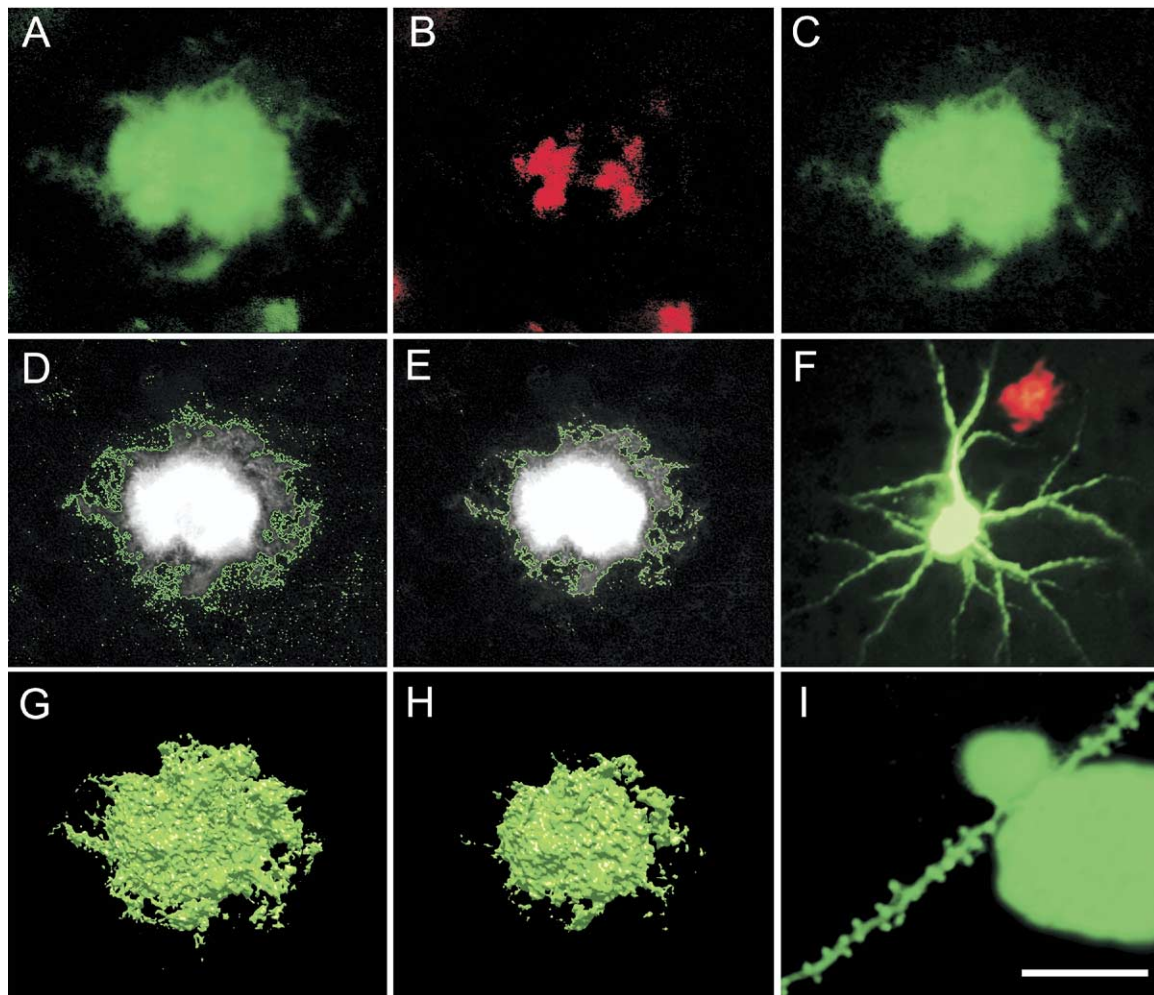
Fig. 12. Senile plaque from an AD case extracted from background autofluorescence and surfaced at two different thresholds using NeuronStudio. (A) Plaque with superimposed autofluorescence. (B) After spectral imaging and linear unmixing, lipofuscin fluorescent signal (red) is separated from that of the plaque. (C) Extracted plaque (green). (D, E, G, H) Comparison of surfaced plaques (G, H) following segmentation with visually determined thresholds (D, E). When a lower threshold is selected (D), the resultant mass is larger and surface rougher (G). When a higher threshold is selected (E), the mass is smaller and the surface less rough (H). The widest diameter of the plaque is approximately 100 μm. (F, I) Effects of local amyloid beta plaque accumulations on dendritic and spine morphology. Dendrites in the vicinity of a plaque are displaced by the plaque (F). Local loss of spines as a dendrite traverses a plaque (I). Image is from a single confocal plane through the periphery of a plaque, so the plaque looks artificially small. Scale bar=150 μm in F; and 10 μm in I. (For interpretation of the references to colour in this figure legend, the reader is referred to the web version of this article.)

DISCUSSION

In this report, we describe a new 3D shape analysis technique, the Rayburst sampling algorithm that uses the intensity information from the 26-connected neighborhood of each voxel to interpolate medial axes, surface thresholds and distance measurements linearly within a voxel. We demonstrate use of Rayburst sampling for dendritic diameter estimation in structures ranging from subcellular through multicellular and network levels. We used these techniques to reconstruct pyramidal neurons from multiple confocal image stacks, and digitize them as a series of generalized cylinders in standard neuroanatomical format. We also use Rayburst sampling to digitize two globally complex network structures: multineuron networks from the hippocampus of eGFP-expressing transgenic mice,

and fluorescently labeled neocortical vascular networks acquired from live mice by MPLSM. These spatially complex structures are skeletonized and digitized in generalized cylindrical format, enabling future analysis of mass distribution and global complexity measures in true 3D. We further demonstrate an application of these approaches to recovering 3D mass distribution and surface roughness of senile plaques from the cerebral cortex of a patient with AD, as an example of a space-filling histopathologic lesion. Finally, we investigate the limits of automated skeletonization methods when tissue is imaged at less than optimal resolution, bit depth and magnification. The robustness of these techniques depends upon the optical resolution, depth of field, pixel size, bit depth and signal–noise ratio of the original images, which can introduce artifactual loops in

tree topology and dendritic breakages. By imaging the same neuron with different modalities, magnifications, resolutions and bit depths, we show that robust recovery of the dendritic tree depends most sensitively upon objective lens magnification, and the n.a. of the lens.

By reconstructing global cellular structures on a microscopic scale these tools will allow, for the first time, model based simulation and evaluation of the *coincident* effects of parameters such as dendritic branching topology and spine geometry, on both global and local scales. Both scales are critical in regulating neuronal dynamics and synaptic plasticity (Magee and Johnston, 1997; Stuart et al., 1997; Matsuzaki et al., 2001; Stuart and Häusser, 2001; Vetter et al., 2001; Yuste and Bonhoeffer, 2001; Henry et al., 2002), however, to date, no tools exist for assessing their combined effects, or their interactions. Research on age-related deficits in cognitive function of humans, non-human primates and rodents demonstrates morphologic changes at both global and local levels but no mechanistic theory currently exists for linking altered function to structural changes.

The approaches outlined in this paper will prove useful in relating functional deficits to morphologic changes at a level that is impossible with current technology, by addressing the *mechanisms* by which altered dendritic structure may lead to memory deficits. With the growing recognition that fine dendritic, spine and network structures are crucial determinants of electrical and biochemical compartmentalization of neural function (Wickens, 1988; Lisman, 1989; Koch and Zador, 1993; Yuste and Bonhoeffer, 2001), development of these tools will impact both the computational neuroscience community directly, as well as neurobiological research in general.

REFERENCES

Abdul-Karim MA, Al-Kofahi K, Brown EB, Jain RK, Roysam B (2003) Automated tracing and change analysis of angiogenic vasculature from *in vivo* multiphoton confocal image time series. Microvasc Res 66:113–125.

Albert MS (1996) Cognitive and neurobiologic markers of early Alzheimer's disease. Proc Natl Acad Sci U S A 93:13547–13551.

Al-Kofahi KA, Lasek S, Szarowski DH, Pace CJ, Nagy G, Turner JN, Roysam B (2003) Rapid automated three-dimensional tracing of neurons from confocal image stacks. IEEE Trans Information Technol Biomed 6:171–187.

Anderson B, Rutledge V (1996) Age and hemisphere effects on dendritic structure. Brain 119:119–1990.

Ascoli GA (2003) Passive dendritic integration heavily affects spiking dynamics of recurrent networks. Neural Netw 16:657–663.

Ashby N, Brittin WE (1986) Thomson's problem. Am J Phys 54:776–777.

Baer SM, Rinzel J (1991) Propagation of dendritic spikes mediated by excitable spines: a continuum theory. J Neurophysiol 65:874–890.

Bailey T, Rivara CB, Rocher AB, Hof PR (2004) The nature and effects of cortical microvascular pathology in aging and Alzheimer's disease. Neurol Res 26:573–578.

Baish JW, Jain RK (2000) Fractals and cancer. Cancer Res 60:3683–3688.

Batchelor MT, Henry BI, Watt SD (1998a) Mean-field analysis of Williams-Bjerknes-type growth. Physica A 256:295–311.

Batchelor MT, Henry BI, Watt SD (1998b) Surface width scaling in noise reduced Eden clusters. Phys Rev E 58:4023–4026.

Bell MA, Ball MJ (1981) Morphometric comparison of hippocampal microvasculature in ageing and demented people: diameters and densities. Acta Neuropathol 53:299–318.

Bloom FE, Young WG, Nimchinsky EA, Hof PR, Morrison JH (1997) Neuronal vulnerability and informatics in human disease. In: Progress in neuroinformatics research, Vol. I: Neuroinformatics: an overview of the Human Brain Project (Koslow SH, Huerta MF, eds), pp 83–123. Mahwah: Lawrence Erlbaum.

Borgefors G (1996) On digital distance transforms in three dimensions. Comput Vision Image Understand 64:368–376.

Borgefors G, Nystrom I, Sanniti Di Baja G (1999) Computing skeletons in three dimensions. Pattern Recog 32:1225–1236.

Bower JM, Beeman D (1998) The book of Genesis: exploring realistic neural systems with the GEneral NEural SImulation System. Springer-Verlag.

Braitenberg V, Braitenberg C (1979) Geometry of orientation columns in the visual cortex. Biol Cybern 33:179–186.

Buée L, Hof PR, Bouras C, Delacourte A, Perl DP, Morrison JH, Fillit HM (1994) Pathological alterations of the cerebral microvasculature in Alzheimer's disease and related dementing disorders. Acta Neuropathol 87:469–480.

Burton BP, McCormick BH, Torp R, Fallon JH (2001) Three-dimensional reconstruction of neuronal forests. Neurocomputing 38–40: 1643–1650.

Cannon RC, Turner DA, Pyapali GK, Wheal HV (1998) An on-line archive of reconstructed hippocampal neurons. J Neurosci Methods 84:49–54.

Carmeliet P (2003) Angiogenesis in health and disease. Nat Med 9:653–660.

Chetelat G, Desgranges B, de la Sayette V, Viader F, Eustache F, Baron JC (2002) Mapping gray matter loss with voxel-based morphometry in mild cognitive impairment. Neuroreport 13: 1939–1943.

Conway JH, Sloane NJA (1993) Sphere packings, lattices and groups. New York: Springer-Verlag.

Cooper DML, Turinsky AL, Sensen CW, Hallgrimsson B (2003) Quantitative 3D analysis of the canal network in cortical bone by micro-computed tomography. Anat Rec B New Anat 274:169–179.

D'Amore JD, Kajdasz ST, McLellan ME, Backsai BJ, Stern EA, Hyman BT (2003) In vivo multiphoton imaging of a transgenic mouse model of Alzheimer's disease reveals marked thioflavine-S associated alterations in neurite trajectories. J Neuropathol Exp Neurol 62:137–145.

de Brabander JM, Kramers RJ, Uylings HB (1998) Layer-specific dendritic regression of pyramidal cells with ageing in the human prefrontal cortex. Eur J Neurosci 10:1261–1269.

Du AT, Schuff N, Amend D, Laaksko MP, Hsi YY, Jagust WJ, Yaffe K, Kramer JH, Reed B, Norman D, Chui HC, Weiner MW (2001) Magnetic resonance imaging of entorhinal cortex and hippocampus in mild cognitive impairment and Alzheimer's disease. J Neurol Neurosurg Psychiatry 71:441–447.

Duan H, He Y, Wicinski B, Morrison JH, Hof PR (2000) Age-related dendrite and spine changes in corticocortically projecting neurons in macaque monkeys. Soc Neurosci Abstr 26:1237

Duan H, Wearne SL, Morrison JH, Hof PR (2002) Quantitative analysis of the dendritic morphology of corticocortical projection neurons in the macaque monkey association cortex. Neuroscience 114:349–359.

Duan H, Wearne SL, Rocher AB, Macedo A, Morrison JH, Hof PR (2003) Age-related morphologic alterations in dendrites and spine densities of corticocortically projecting neurons in macaque monkeys. Cereb Cortex 13:950–961.

Einstein AJ, Gil J (1998) Self-affinity and lacunarity of chromatin texture in benign and malignant breast epithelial cell nuclei. Phys Rev Lett 80:397–400.

Einstein AJ, Wu HS, Sanchez M, Gil J (1998) Fractal characterization of chromatin appearance for diagnosis in breast cytology. J Pathol 185:366–381.

Euler T, Denk W (2001) Dendritic processing. Curr Opin Neurobiol 11:415–422.

Fischer VW, Siddiqi A, Yusufaly Y (1990) Altered angioarchitecture in selected areas of brains with Alzheimer's disease. Acta Neuropathol 79:672–679.

Fridman Y, Pizer SM, Aylward S, Bullitt E (2004) Extracting branching tubular object geometry via cores. Med Image Anal 8:169–176.

Gazit Y, Baish JW, Safabaksh N, Leunig M, Baxter LT, Jain RK (1997) Fractal characteristics of tumor vascular architecture during tumor growth and regression. Microcirculation 4:395–402.

Gazit Y, Berk DA, Leunig M, Baxter LT, Jain RK (1995) Scale-invariant behavior and vascular network formation in normal and tumor tissue. Phys Rev Lett 75:2428–2431.

Giraldo FX (1997) Lagrange-Galerkin methods on spherical geodesic grids. J Comput Phys 136:197–213.

Hao J, Rapp PR, Leffler A, Leffler S, Janssen WG, McKay H, Roberts JH, Wearne SL, Hof PR, Morrison JH (2004) Long-term cyclic estrogen replacement increases spine density in the prefrontal cortex of aged ovariectomized rhesus monkeys. Soc Neurosci Abstr 30:72.7 (http://www.sfn.org).

Harris KM, Jensen FE, Tsao B (1992) Three-dimensional structure of dendritic spines and synapses in rat hippocampus (CA1) at postnatal day 15 and adult ages: implications for the maturation of synaptic physiology and long-term potentiation. J Neurosci 12:2685–2705.

Harris KM, Kater SB (1994) Dendritic spines: cellular specializations imparting both stability and flexibility to synaptic function. Annu Rev Neurosci 17:341–371.

Harris KM, Stevens JK (1988) Dendritic spines of rat cerebellar Purkinje cells: serial electron microscopy with reference to their biophysical characteristics. J Neurosci 8:4455–4469.

Häusser M, Mel BW (2003) Dendrites: bug or feature? Curr Opin Neurobiol 13:372–383.

He W, Hamilton TA, Cohen AR, Holmes TJ, Pace C, Szarowski DH, Turner DA, Roysam B (2003) Automated three-dimensional tracing of neurons in confocal and brightfield images. Microsc Microanal 9:296–310.

Henry BI, Hof PR, Rothnie P, Wearne SL (2002) Fractal analysis of aggregates of non-uniformly sized particles: an application to macaque monkey cortical pyramidal neurons. In: Emergent nature: patterns, growth and scaling in the sciences (Novak MM, ed), pp 65–75. New Jersey: World Scientific Publishing.

Hill S (1994) Trilinear interpolation. In: Graphics gems IV (Heckbert PS, ed), pp 521–525. San Diego: Academic Press.

Hines ML (1994) The NEURON simulation program. In: Neural network simulation environments (Skrzypek J, ed), pp 147–163. Norwell, MA: Kluwer.

Hof PR, Morrison JH (2004) The aging brain: morphomolecular senescence of cortical circuits. Trends Neurosci 27:607–613.

Holmes WR (1989) The role of dendritic diameter in maximizing the effectiveness of synaptic inputs. Brain Res 478:127–137.

Holmes WR, Rall W (1992) Estimating the electrotonic structure of neurons with compartmental models. J Neurophysiol 68:1438–1452.

Jacobs B, Schall M, Prather M, Kapler E, Driscoll L, Baca S, Jacobs J, Ford K, Wainwright M, Treml M (2001) Regional dendritic and spine variation in human cerebral cortex: a quantitative Golgi study. Cereb Cortex 11:558–571.

Jain RK (2002) Angiogenesis and lymphangiogenesis in tumors: insights from intravital microscopy. Cold Spring Harbor Symp Quant Biol 67:239–248.

Jain RK (2003) Molecular regulation of vessel maturation. Nat Med 9:685–693.

Jain RK, Munn LL, Fukumura D (2002) Dissecting tumor pathophysiology using intravital microscopy. Nat Rev Cancer 2:266–276.

Kabaso D, Henry BI, Hof PR, Wearne SL (2003) Effects on action potential backpropagation of age-related changes in dendritic branching and spine densities of neocortical pyramidal neurons in macaque monkey. Program Number: 810.1, 2003 Abstract Viewer/ Itinerary Planner, Washington, DC. Soc Neurosci Abstr (http://www.sfn.org).

Keuker JIH, Luiten PGM, Fuchs E (2000) Capillary changes in hippocampal CA1 and CA3 areas of the aging rhesus monkey. Acta Neuropathol 100:665–672.

Knowles RB, Wyart C, Buldyrev SV, Cruz L, Urbanc B, Hasselmo ME, Stanley HE, Hyman BT (1999) Plaque-induced neurite abnormalities: implications for disruption of neural networks in Alzheimer's disease. Proc Natl Acad Sci U S A 96:5274–5279.

Koch C (1999) Biophysics of computation: information processing in single neurons. New York: Oxford University Press.

Koch C, Segev I (2000) The role of single neurons in information processing. Nat Neurosci 3:1171–1177.

Koch C, Zador A (1993) The function of dendritic spines: devices subserving biochemical rather than electrical compartmentalization. J Neurosci 13:413–422.

Koh IYY, Lindquist WB, Zito K, Nimchinsky EA, Svoboda K (2002) An image analysis algorithm for the fine structure of neuronal dendrites. Neural Comput 14:1283–1310.

Krichmar JL, Nasuto SJ, Scorcioni R, Washington SD, Ascoli GA (2002) Effects of dendritic morphology on CA3 pyramidal cell electrophysiology: a simulation study. Brain Res 941:11–28.

Le R, Cruz L, Urbanc B, Knowles RB, Hsiao-Ashe K, Duff K, Irrizarry MC, Stanley HE, Hyman BT (2001) Plaque-induced abnormalities in neurite geometry in transgenic models of Alzheimer's disease: implications for neural system disruption. J Neuropathol Exp Neurol 60:753–758.

Lee TC, Kashyap RL, Chu C (1994) Building skeleton models via 3-D medial surface/axis thinning algorithms. CVGIP: Graph. Models Image Process 56:462–478.

Lefebvre F, Benali H, Gilles R, Kahn E, DiPaola R (1995) A fractal approach to the segmentation of microcalcifications in digital mammograms. Med Phys 22:381–390.

Lisman JE (1989) A mechanism for the Hebb and anti-Hebb processes underlying learning and memory. Proc Natl Acad Sci U S A 86:9574–9578.

Magee JC, Johnston DA (1997) A synaptically controlled, associative signal for Hebbian plasticity in hippocampal neurons. Science 275:209–213.

Magistretti PJ (2000) Cellular bases of functional brain imaging: insights from neuron-glia metabolic coupling. Brain Res 886:108–112.

Magistretti PJ, Pellerin L (1999) Cellular mechanisms of brain energy metabolism and their relevance to functional brain imaging. Phil Trans R Soc Lond B 354:1155–1163.

Mainen ZF, Sejnowski TJ (1996) Influence of dendritic structure on firing pattern in model neocortical neurons. Nature 382:363–366.

Mandelbrot B, Vicsek T (1989) Directed recursive models for fractal growth. J Phys A Math Gen 23:L377–L383.

Matsuzaki M, Ellis-Davies GCR, Nemoto T, Miyashita Y, Iino M, Kasai H (2001) Dendritic spine geometry is critical for AMPA receptor expression in hippocampal CA1 pyramidal neurons. Nat Neurosci 4:1086–1092.

McCormick BH (1999) Design of a brain tissue scanner. Neurocomputing 26- 27:1025–1032.

Messerli M (2000) NeuronTracer reference manual V. 1.0. Zurich: Bitplane AG.

Mountcastle VB (1978) An organizing principle for cerebral function: the unit module and the distributed system. In: The mindful brain (Edelman GM, Mountcastle VB, eds), pp 36–41. Cambridge: MIT Press.

Mountcastle VB (1997) The columnar organization of the neocortex. Brain 120:701–722.

Nedergaard M, Ransom B, Goldman SA (2003) New roles for astrocytes: redefining the functional architecture of the brain. Trends Neurosci 26:523–530.

Nikolaidis N, Pitas I (2001) 3-D image processing algorithms. New York: John Wiley and Sons, Inc.

Nimchinsky EA, Sabatini BL, Svoboda K (2002) Structure and function of dendritic spines. Annu Rev Physiol 64:313–353.

Page TL, Einstein M, Duan H, He Y, Flores T, Rolshud D, Erwin JM, Wearne SL, Morrison JH, Hof PR (2002) Morphological alterations in neurons forming corticocortical projections in the neocortex of aged patas monkeys. Neurosci Lett 317:37–41.

Perl DP, Good PF, Bussière T, Morrison JH, Erwin JM, Hof PR (2000) Practical appoaches to stereology in the setting of aging- and disease-related brain banks. J Chem Neuroanat 20:7–19.

Pohlman S, Powell K, Obuchowski NA, Chilcote WA, Grundfest-Broniatowski S (1996) Quantitative classification of breast tumors in digitized mammograms. Med Phys 23:1337–1345.

Radley JJ, Rocher AB, Miller M, Janssen WGM, Hof PR, McEwen BS, Morrison JH (2005) Chronic behavioral stress induces apical dendritic spine loss in pyramidal neurons of the rat medial prefrontal cortex. Cereb Cortex, in press.

Rall W (1962) Theory of physiological properties of dendrites. Ann N Y Acad Sci 96:1071–1092.

Rall W (1964) Theoretical significance of dendritic trees for input-output relations. In: Neural theory and modeling (Reiss pp. RF, ed), 73–79. Stanford: Stanford University Press.

Rockland KS, Ichinohe N (2004) Some thoughts on cortical minicolumns. Exp Brain Res 158:265–277.

Rodriguez A, Ehlenberger D, Kelliher KT, Einstein M, Henderson SC, Hof PR, Wearne SL (2003a) Automated reconstruction of 3D neuronal morphology from laser scanning microscopy images. Methods 30:94–105.

Rodriguez A, Ehlenberger D, Kelliher KT, Henderson SC, Hof PR, Wearne SL (2003b) Automated dendritic arbor extraction and surface area estimation from confocal and multiphoton imaged data. Soc Neurosci Abstr 30:428.18

Romijn HJ, van Uum JFM, Breedijk I, Emmering J, Radu I, Pool CW (1999) Double immunolabeling of neuropeptides in the human hypothalamus as analyzed by confocal laser scanning fluorescence microscopy. J Histochem Cytochem 47:229–236.

Sander LM, Cheng ZM, Richter R (1983) Diffusion-limited aggregation in three dimensions. Phys Rev B 28:6394–6396.

Schmitt S, Evers JF, Duch C, Scholz M, Obermayer K (2004) New methods for the computer-assisted 3-D reconstruction of neurons from confocal image stacks. Neuroimage 23:1283–1298.

Small SA, Tsai WY, DeLaPaz R, Mayeux R, Stern Y (2002) Imaging hippocampal function across the human life span: is memory decline normal or not? Ann Neurol 51:290–295.

Stern EA, Backsai BJ, Hickey GA, Attenello FJ, Lombardo JA, Hyman BT (2004) Cortical synaptic integration in vivo is disrupted by amyloid-beta plaques. J Neurosci 24:4535–4540.

Stratford K, Mason A, Larkman A, Major G, Jack J (1989) The modeling of pyramidal neurons in the visual cortex. In: The computing neuron (Durbin R, Miall C, Mitchison G, eds), pp 296–321. London: Addison-Wesley.

Streekstra GJ, Smeulders AWM, van den Boomgaard R (1999) Tracing of curvilinear structures in 3D images with single scale diameter measurement. Proceedings of the Second International Conference on Scale-Space Theories in Computer Vision, pp. 501–506.

Streekstra GJ, Smeulders AWM, van den Boomgaard R (2000) Scale dependent differential geometry for the measurement of center line and diameter in 3D curvilinear structures. 6th European Conference on Computer Vision 2000, Dublin, Ireland, pp. 856–870.

Stuart G, Schiller J, Sakmann B (1997) Action potential initiation in neocortical pyramidal neurons. J Physiol 505:617–632.

Stuart G, Spruston N, Häusser M, eds (1999) Dendrites. Oxford: Oxford University Press.

Stuart GJ, Häusser M (2001) Dendritic coincidence detection of EPSPs and action potentials. Nat Neurosci 4:63–70.

Surkis A, Peskin CS, Tranchina D, Leonard CS (1998) Recovery of cable properties through active and passive modeling of subthreshold membrane responses from laterodorsal tegmental neurons. J Neurophysiol 80:2593–2607.

Tombre K, Ah-Soon C, Dosch P, Masini G, Tabbone S (2000) Stable and robust vectorization: how to make the right choices. In: Graphics recognition: recent advances. Lecture notes in computer science (Chhabra AK, Dori D, eds), pp 3–19. Springer-Verlag.

Tsai J, Grutzendler J, Duff K, Gan W-B (2004) Fibrillar amyloid deposition leads to local synaptic abnormalities and breakage of neuronal branches. Nat Neurosci 7:1181–1183.

Tsay D, Yuste R (2001) Role of dendritic spines in action potential backpropagation: A numerical simulation study. J Neurophysiol 88:2834–2845.

Urbanc B, Cruz L, Le R, Sanders J, Hsiao-Ashe K, Duff K, Stanley HE, Irrizarry MC, Hyman BT (2002) Neurotoxic effects of thioflavin S positive amyloid deposits in transgenic mice and Alzheimer's disease. Proc Natl Acad Sci U S A 99:13990–13995.

van Pelt J, van Ooyen A, Uylings HBM (2001) The need for integrating neuronal morphology databases and computational environments in exploring neuronal structure and function. Anat Embryol 204:255–265.

Vetter P, Roth A, Häusser M (2001) Propagation of action potentials in dendrites depends on dendritic morphology. J Neurophysiol 85:926–937.

Westpfahl DJ, Coleman PH, Alexander J, Tongue T (1999) The geometry of the H1 of several members of the M81 group: the H1 is fractal. Astronom J 117:868–880.

Whyte LL (1952) Unique arrangement of points on a sphere. Am Math Monthly 59:606–611.

Wickens J (1988) Electrically coupled but chemically isolated synapses: dendritic spines and calcium in a rule for synaptic modification. Prog Neurobiol 31:507–528.

Wilson CJ (1988) Cellular mechanisms controlling the strength of synapses. J Electron Microsc Tech 10:293–313.

Witten TA, Sander LM (1981) Diffusion limited aggregation, a kinetic critical phenomenon. Phys Rev Lett 47:1400–1403.

Witten TA, Sander LM (1983) Diffusion-limited aggregation. Phys Rev B 27:5686

Wu C-C, Reilly JF, Young WG, Morrison JH, Bloom FE (2004) High-throughput morphometric analysis of individual neurons. Cereb Cortex 14:543–554.

Yuste R, Bonhoeffer T (2001) Morphological changes in dendritic spines associated with long-term synaptic plasticity. Annu Rev Neurosci 24:1071–1089.